DEVELOPMENTAL BIOLOGY

Transcriptional regulation by the NSL complex enables diversification of IFT functions in ciliated versus nonciliated cells

Tsz Hong Tsang[1,2,3], Meike Wiese[1], Martin Helmstädter[4], Thomas Stehle[1], Janine Seyfferth[1], Maria Shvedunova[1], Herbert Holz[1], Gerd Walz[4,5,6], Asifa Akhtar[1,6]*

Members of the NSL histone acetyltransferase complex are involved in multiorgan developmental syndromes. While the NSL complex is known for its importance in early development, its role in fully differentiated cells remains enigmatic. Using a kidney-specific model, we discovered that deletion of NSL complex members KANSL2 or KANSL3 in postmitotic podocytes led to catastrophic kidney dysfunction. Systematic comparison of two primary differentiated cell types reveals the NSL complex as a master regulator of intraciliary transport genes in both dividing and nondividing cells. NSL complex ablation led to loss of cilia and impaired sonic hedgehog pathway in ciliated fibroblasts. By contrast, nonciliated podocytes responded with altered microtubule dynamics and obliterated podocyte functions. Finally, overexpression of wild-type but not a double zinc finger (ZF-ZF) domain mutant of KANSL2 rescued the transcriptional defects, revealing a critical function of this domain in NSL complex assembly and function. Thus, the NSL complex exhibits bifurcation of functions to enable diversity of specialized outcomes in differentiated cells.

INTRODUCTION

The fine-tuning of acetylation requires a balanced interplay between the histone acetyltransferases (HATs) and histone deacetylases (HDACs), and the dysregulation of acetylation is associated with many diseases (*1*–*3*). For example, HATs such as *MOF* (also known as *KAT8*), *CBP*, and *EP300* have been implicated in developmental disorders and intellectual disability (*4*–*7*). Additionally, mutations in *MSL3* and *KANSL1*, members of the MOF-interacting male-specific lethal (MSL) and nonspecific lethal (NSL) complexes, respectively, are also associated with multiorgan developmental syndromes characterized by intellectual disability (*8*, *9*).

Studies have shown that HATs are essential during early embryonic development, as mouse models with genetic deletion of *Mof*, *Cbp*, *p300*, and many others show lethality at embryonic stages (*10*, *11*). However, their functions later in development and during the adult stage are less defined, and it has become increasingly clear that the roles of HATs could be highly sensitive to molecular as well as cellular contexts (*1*). For example, MOF substrate specificity is dependent on the molecular complex it is associated with. When associated with the MSL complex, MOF achieves an extremely high specificity for H4K16ac, but when partnered with the NSL complex, it has been shown to have a broader substrate repertoire, acetylating additional H4 residues H4K5ac, H4K8ac, and H4K12ac, as well as nonhistone proteins (*9*, *12*–*14*). At the molecular level, MOF associates exclusively with either the MSL or the NSL complex, meaning MOF's choice of partner is likely to be a key determinant of its function (*15*, *16*). In the context of the NSL complex, it has been shown that the NSL complex is a transcriptional activator that binds promoters and promotes the recruitment of RNA polymerase II and the NURD nucleosome remodeler complex to target genes (*17*–*22*). Furthermore, the H4 acetylation marks mediated by the NSL complex have also been found to promote the recruitment of BRD4 (*23*). In addition, the NSL complex has been shown to regulate various tissue- and cell type–specific functions (*6*, *24*–*26*). For example, NSL complex depletion causes defects in red blood cell development due to deregulation of the hematopoiesis regulator RUNX1, while in embryonic neurons, NSL complex removal led to changes in lipid metabolism pathways and eventually to a breakdown of the neurovasculature (*24*, *26*).

We have previously reported that podocyte-specific deletion of *Mof* exacerbates the podocyte injury phenotype elicited by doxorubicin, but it is uncertain whether and how the NSL complex might be involved (*27*). Furthermore, the direct chromatin targets of MOF and the NSL complex in podocytes have not been characterized before. Within the kidney glomeruli, podocytes are one of the most important cell types whose injury is a pivotal event leading to proteinuric kidney disease, glomerulosclerosis, and loss of renal functions (*28*). Podocytes are fully differentiated, highly specialized, and postmitotic cells with a limited capacity for regeneration. They are the major filtration units of the glomeruli, and their constant exposure to physical forces demands a complex cellular morphology with a sophisticated cytoskeletal network (*29*). A typical podocyte consists of a cell body, primary processes that consist primarily of microtubules, and branching secondary processes (also known as foot processes) that are enriched in actin (*30*, *31*). Slit diaphragms, specialized cell-cell junctions found between two interdigitating podocyte foot processes, function together with the glomerular basement membrane to form the glomerular filtration barrier (*32*–*34*). Therefore, the proper

[1]Max Planck Institute of Immunobiology and Epigenetics, 79108 Freiburg, Germany. [2]Faculty of Biology, University of Freiburg, 79104 Freiburg, Germany. [3]International Max Planck Research School for Molecular and Cellular Biology (IMPRS-MCB), 79108 Freiburg, Germany. [4]Department of Medicine IV, University Freiburg Medical Center, Faculty of Medicine, University of Freiburg, Hugstetter Strasse 55, 79106 Freiburg, Germany. [5]BIOSS Centre for Biological Signalling Studies, University of Freiburg, Schänzlestrasse 18, 79104 Freiburg, Germany. [6]CIBSS Centre for Integrative Biological Signalling Studies, University of Freiburg, Schänzlestrasse 18, 79104 Freiburg, Germany.
*Corresponding author. Email: akhtar@ie-freiburg.mpg.de

maintenance of cytoskeletal structures in podocytes is crucial for their function and mutations in genes involved in cytoskeletal functions are often implicated in glomerular diseases (*29*, *35*). The NSL complex protein KANSL3 has previously been identified to be a mitosis-specific microtubule minus-end binder (*36*). However, whether the NSL complex plays any role in regulating microtubule function in noncycling interphase cells remains unexplored.

Here, we investigated the role of KANSL2 and KANSL3, protein members unique to the NSL complex, in both glomerular podocytes and mouse embryonic fibroblasts (MEFs). Mice with podocyte-specific deletion of KANSL2 or KANSL3 showed severe glomerulosclerosis and premature lethality. We reveal a critical role for the NSL complex in transcription of ciliary genes of both ciliated and nonciliated cells, and uncover a context-specific diversification of function for the NSL complex–mediated regulation of ciliary genes according to the ciliation status of the affected cell type. In ciliated cells (MEFs), NSL complex–mediated regulation of ciliary genes is critical for cilia assembly and sonic hedgehog (shh) signaling, whereas in nonciliated podocytes we implicate NSL complex–mediated regulation of ciliary genes in organization of the microtubule cytoskeleton, which likely led to the podocytopathy and kidney defects observed upon podocyte-specific deletion of KANSL2 and KANSL3 in vivo.

RESULTS

KANSL2 and KANSL3 depletion causes severe glomerulopathy

To evaluate the role of KANSL2 and KANSL3 in terminally differentiated podocytes, we crossed the *Kansl2*$^{fl/fl}$ and *Kansl3*$^{fl/fl}$ mice with mice expressing Cre under the control of the podocyte-specific *Nphs2* promoter (Nphs2-Cre, or nCre) (Fig. 1A) (*26*, *37*). The *Nphs2* promoter exerts its activity from embryonic day 14.5 onward and is expressed only in podocytes during the late capillary loop stage, the penultimate stage of glomerular development when the characteristic mature ultrastructure of podocytes required for proper filtration has been properly formed (*37*, *38*). Mice with loss of KANSL2 (Kansl2-pKO) and KANSL3 (Kansl3-pKO) in podocytes showed no notable difference in either urinary albumin:creatinine ratio or body weight from 0 to 2 weeks of age compared to wild-type (WT) nCre animals (Fig. 1, B and C). However, they progressively developed substantial proteinuria as measured by albumin:creatinine ratio from 3 and 4 weeks of age, respectively (Fig. 1B). Kansl2-pKO and Kansl3-pKO mice exhibited significant weight loss compared to WT nCre animals from 5 and 6 weeks of age, respectively (Fig. 1C). This phenotype was followed by early lethality with a median survival age of 7.5 and 10 weeks for Kansl2-pKO and Kansl3-pKO, respectively (Fig. 1D).

At 6 weeks of age, a difference in size between Kansl2-pKO and nCre animals became obvious, and kidneys from Kansl2-pKO animals appeared consistently paler than those from littermate controls (Fig. 1E). Histological analysis by periodic acid–Schiff (PAS) staining revealed severe glomerulosclerosis accompanied by tubular dilation and tubular protein cast for both Kansl2-pKO and Kansl3-pKO mice at 6 weeks of age (Fig. 1F). Sirius red staining further revealed fibrosis across kidney tissues, suggesting that by 6 weeks of age secondary defects were already evident (Fig. 1G). In addition, we compared the weights of various internal organs of Kansl2-pKO animals to littermate controls at 6 weeks of age (fig. S1, A and B). While kidney weight remained proportional to body weight, we observed significant relative weight reduction of both thymus and spleen, although Nphs2-Cre has no reported activity there (*39*). Premature immune aging, with symptoms including thymus atrophy, is well documented in patients suffering from chronic kidney diseases (*40*, *41*). In line with this, our observation suggested secondary phenotypes in thymus and spleen caused by primary kidney defect already by 6 weeks of age. To confirm the lack of Cre activities in these organs, we made use of the mTomato$^{fl/fl}$mGFP (mTmG) reporter in which Cre-positive cell types were labeled with green fluorescent protein (GFP) and the Cre-negative cell types were labeled with mTomato. GFP signals were only observed in glomerular podocytes, while none was observed in either thymus or spleen (fig. S1C). This confirmed the lack of Cre-mediated deletion in either thymus or spleen, and confirmed that the phenotypes we observed in these organs were secondary to that of the primary podocyte injury caused by loss of KANSL2 or KANSL3.

To assess the morphology of podocyte foot processes during early stages of disease progression, morphological analyses were done at higher magnification using an electron microscope at 3 weeks of age to look at individual glomeruli as well as podocytes. Scanning electron microscopy (SEM) revealed a simplification of the interdigitation pattern between the foot processes of neighboring podocytes in both Kansl2-pKO and Kansl3-pKO glomeruli (Fig. 1H, top panel). Transmission electron microscopy (TEM) further revealed the effacement of podocyte foot processes, a hallmark of podocytopathy, as well as a reduction in the density of slit diaphragms in Kansl2-pKO and Kansl3-pKO mice (Fig. 1, H, bottom panel, and I). These observations confirmed that the NSL complex members KANSL2 and KANSL3 are important in podocyte homeostasis and that the removal of these proteins causes primary podocytopathy.

Podocyte-specific loss of KANSL2 and KANSL3 causes down-regulation of genes related to cilia and microtubule-based transport

To identify the molecular changes associated with the severe physiological phenotype observed following podocyte-specific deletion of the NSL complex, we performed transcriptome analyses on podocytes isolated from these mice. To genetically label the podocytes, we crossed nCre, Kansl2-pKO, and Kansl3-pKO mice with mTmG reporter mice (*27*). We then sorted podocytes with fluorescence-activated cell sorting (FACS) and performed RNA sequencing (RNA-seq) (Fig. 2A). Interactive Genome Viewer (IGV) tracks and Western blot confirmed a complete knockout (KO) of either KANSL2 (fig. S1, D and F) or KANSL3 (fig. S1, E and G) in the respective models. As shown by the principal components analysis (PCA), Kansl2-pKO and Kansl3-pKO podocytes showed similar molecular signatures but were distinct from nCre (fig. S2A). Podocytes isolated from Kansl2-pKO and Kansl3-pKO mice displayed 4441 and 4304 deregulated genes, respectively (Fig. 2B, fig. S2B, and tables S1 and S2). Podocyte cell identity was maintained despite the substantial transcriptome changes, as expression of characteristic podocyte cell markers including *Wt1*, *Cd2ap*, *Podxl*, *Pdpn*, *Actn4*, *Nphs1*, *Nphs2*, and *Synpo* remained mostly unaffected (tables S1 and S2).

We next asked whether the dysregulated genes have any concerted biological functions by conducting unbiased geneset enrichment

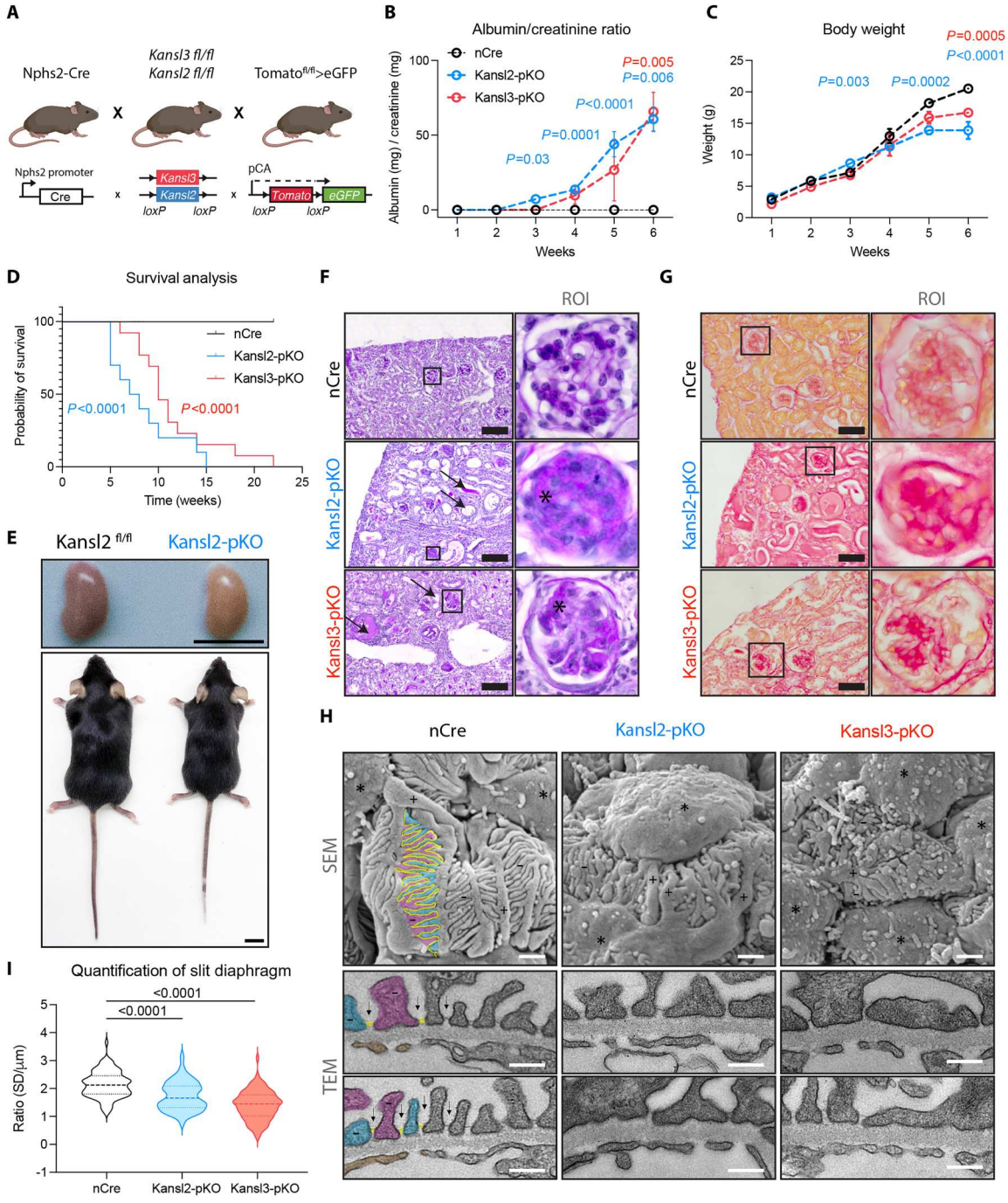

Fig. 1. KANSL2 and KANSL3 depletion causes severe glomerulopathy. (**A**) *Kansl2*$^{fl/fl}$ and *Kansl3*$^{fl/fl}$ mice were crossed to nCre mice to generate podocyte-specific *Kansl2* (Kansl2-pKO) or *Kansl3* (Kansl3-pKO) KO mice. When necessary, mice were further crossed with mTmG mice to genetically label podocytes. (**B**) Urinary albumin: creatinine ratios from nCre, Kansl2-pKO, and Kansl3-pKO mice (n = 3 to 15 per group per time point). Data are presented as means ± SEM and were analyzed using the Kruskal-Wallis test followed by Dunn's multiple comparisons as post hoc test. (**C**) Body weight of nCre, Kansl2-pKO, and Kansl3-pKO mice (n = 3 to 20 per group per time point). Data are presented as means ± SEM and were analyzed using the ordinary one-way analysis of variance (ANOVA) followed by Tukey's multiple-comparison test. (**D**) Kaplan-Meier survival curve of nCre, Kansl2-pKO, and Kansl3-pKO mice (n = 10 to 13). Data were analyzed by the log-rank (Mantel-Cox) test. (**E**) Representative photo of kidney (top) and body (bottom) from 6-week-old littermate control (left) and Kansl2-pKO (right) mice (scale bar, 1 cm). (**F** and **G**) PAS (F) and Sirius red (G) staining of kidney sections from 6-week-old nCre, Kansl2-pKO, and Kansl3-pKO mice [glomerulosclerosis (asterisks), tubular protein casts with tubular dilatation (arrows); scale bar, 100 μm]. (**H**) SEM (top) and TEM (bottom) of nCre, Kansl2-pKO, and Kansl3-pKO kidneys. (Top) Simplification of the secondary foot process pattern was evident in both Kansl2-pKO and Kansl3-pKO glomeruli by 3 weeks of age [podocyte cell body (asterisk), primary foot process (+), secondary foot process (cyan and magenta; –), slit diaphragms (yellow); scale bar, 1 μm]. (Bottom) Foot process effacement results in a reduction of slit diaphragms in both Kansl2-pKO and Kansl3-pKO glomeruli [secondary foot process (cyan and magenta, –), slit diaphragms (arrows); scale bar, 250 nm]. (**I**) Quantification of TEM in (H) (n = 90 micrographs quantified, n = 3 glomeruli per mouse per genotype). Data were analyzed using the ordinary one-way ANOVA followed by Tukey's multiple-comparison test.

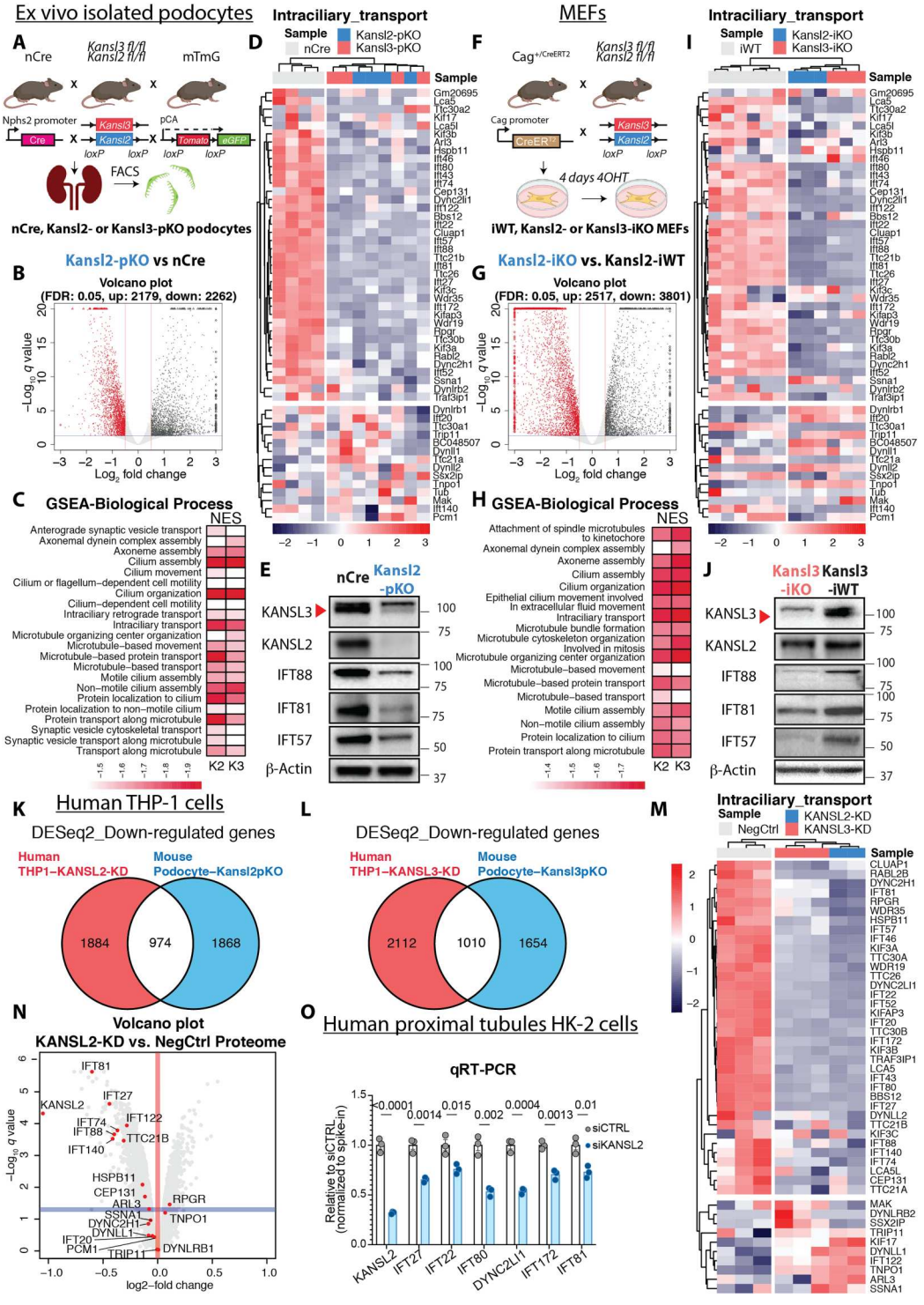

Fig. 2. NSL complex depletion leads to down-regulation of genes in cilia- and microtubule-related pathways. (**A**) Model for isolation of podocytes genetically tagged with mTmG. (**B**) Volcano plot showing the number of differentially expressed genes in Kansl2-pKO versus nCre podocytes [false discovery rate (FDR) < 0.05, log2[fold change] > |0.5|]. (**C**) Heatmap of normalized expression score (NES) from all cilia- and microtubule-related GO-BP terms that appear in the GSEA analysis of either Kansl2-pKO or Kansl3-pKO podocytes. (**D**) Heatmap of *z* scores from genes in the GO term intraciliary transport in podocytes. (**E**) Western blot of KANSL2, KANSL3, and IFT proteins on lysates of podocytes. The red arrowhead points to the specific KANSL3 band. The same Western blot is shown in fig. S1F. (**F**) Model for isolation and culture of MEFs. (**G**) Volcano plot showing the number of differentially expressed genes in Kansl2-iKO MEFs versus the Kansl2-iWT controls (FDR < 0.05, log2[fold change] > |0.5|). (**H**) Heatmap of NES from all cilia- and microtubule-related GO-BP terms that appear in the GSEA analysis of either Kansl2-iKO or Kansl3-iKO MEFs. (**I**) Heatmap of *z* scores from genes in the GO term intraciliary transport in MEFs. (**J**) Western blot of KANSL2, KANSL3, and IFT proteins on MEF lysates. The red arrowhead points to the specific KANSL3 band. (**K** and **L**) Venn diagram showing down-regulated genes (FDR < 0.05, log2[fold change] < 0) in both Kansl2-pKO mouse podocytes and KANSL2-KD human THP-1 cells (K), or in both Kansl3-pKO podocytes and KANSL3-KD THP-1 cells (L). (**M**) Heatmap of *z* scores from genes in the GO term intraciliary transport in THP-1 cells. (**N**) Volcano plot of proteomics data comparing KANSL2-KD versus control THP-1 cells. Proteins within the GO term intraciliary transport as well as KANSL2 are annotated and highlighted in red. (**O**) qRT-PCR of intraciliary transport genes in HK-2 cells transfected with siCTRL or siKANSL2 siRNA ($n = 3$ per group). Data are presented as means ± SEM and were analyzed using a two-tailed Student's *t* test.

analysis (GSEA). We focused on the gene ontology (GO) terms with a negative normalized enrichment score (NES), as they were most likely to represent direct targets of the NSL complex, a transcriptional activator. GSEA revealed that GO terms related to cilia were among the most down-regulated terms in both Kansl2-pKO and Kansl3-pKO podocytes (fig. S2, C and D). This result was totally unexpected, since the terminally differentiated podocytes have been reported to lack cilia (*42*). Furthermore, the NSL complex has not been implicated in regulating transcription of cilia-related genes previously. Since cilia are microtubule-enriched structures, we compared all the GO terms related to cilia and microtubules that appeared in either the GSEA for Kansl2-pKO or Kansl3-pKO (Fig. 2C). We observed very similar GO terms in both KOs, although in general more down-regulated terms as well

as a more negative NES were observed in Kansl2-pKO compared to Kansl3-pKO, consistent with the animal phenotypes observed earlier. Using an alternative approach, we asked how many down-regulated genes overlapped between Kansl2-pKO and Kansl3-pKO and what their functions were, as these genes are more likely to contribute to the phenotype (fig. S2E). A total of 1592 (~70%) genes were down-regulated in both Kansl2-pKO and Kansl3-pKO podocytes. Analysis of this gene set revealed significant enrichment for multiple GO terms related to cilia-related functions. Together, this confirmed that depletion of either the NSL complex member KANSL2 or KANSL3 in podocytes leads to transcription down-regulation of cilia-related genes.

We were very intrigued by the finding that the NSL complex regulated cilia-related genes in nonciliated podocytes. A large number of genes are involved in cilia formation and its regulation, some of which could be associated with a wide variety of cellular functions outside of their ciliary contexts (*43*, *44*). As the cilia-related terms scored in our GSEA analysis include genes with functions as disparate as cilium organization and microtubule-based transport, we wanted to stratify them to try to get a more detailed insight into which specific cilia-related functions were most affected by podocyte-specific *Kansl2* and *Kansl3* KO. To achieve this, we first generated a heatmap comparing all genes in the more inclusive term "Cilia organization" (fig. S2F). Hierarchical clustering revealed that cluster 2 (n = 155) displayed a Kansl2-pKO– and Kansl3-pKO–specific loss of gene expression. Enriched GO terms analysis of cluster 2 revealed enrichment of multiple terms related to protein transport, including the GO term "intraciliary transport" (fig. S2G), which was also present in earlier analyses (Fig. 2C and fig. S2, C to E). Most genes in the GO term intraciliary transport are down-regulated in Kansl2-pKO and Kansl3-pKO podocytes (Fig. 2D). This included genes encoding components of the intraflagellar transport (IFT) complexes, such as *Ift81*, *Ift57*, and *Ift88*. The NSL complex–mediated transcriptional down-regulation of these genes is also reflected in the reduction of these components at the protein level (Fig. 2E). We observed that the removal of KANSL2 also leads to a reduction of KANSL3 at the protein level, although *Kansl3* is transcriptionally unaffected in Kansl2-pKO podocytes. To conclude, the removal of KANSL2 or KANSL3 in podocytes led to a large-scale transcriptomic down-regulation of multiple cellular processes, with genes involved in intraciliary transport showing the most prominent and consistent effect in both pKOs.

Transcriptional regulation of intraciliary transport genes is a core function of the NSL complex in both actively dividing and postmitotic cells

The NSL complex had been shown previously to be capable of regulating both ubiquitous and cell type–specific genes (*45*). We therefore wondered if the observed down-regulation of intraciliary transport genes upon ablation of NSL complex members was specific to postmitotic podocytes. To this end, we generated MEFs from *Kansl2*$^{fl/fl}$ (Kansl2-iWT), *Kansl2*$^{fl/fl}$ *Cag-Cre-ERT2*$^{T/+}$ (Kansl2-iKO), *Kansl3*$^{fl/fl}$ (Kansl3-iWT), and *Kansl3*$^{fl/fl}$ *Cag-Cre-ERT2*$^{T/+}$ (Kansl3-iKO) embryos where Cre expression can be induced by 4-hydroxy-tamoxifen treatment (4OHT) (Fig. 2F). MEFs of each genotype were treated with 2 μM 4OHT for 4 days to induce KO. RNA-seq experiments again revealed a strong transcriptomic perturbation upon removal of either KANSL2 or KANSL3 (Fig. 2G; fig. S3, A and B; and tables S3 and S4). By GSEA analysis, we again identified down-regulation of cilia- and microtubule-related GO terms in MEFs, including intraciliary transport (Fig. 2H). We next overlapped the genes down-regulated in both Kansl2-iKO and Kansl3-iKO MEFs with those deregulated in both Kansl2-pKO and Kansl3-pKO podocytes (fig. S3C). Genes down-regulated preferentially in podocytes were enriched for noncoding RNA processing, while those specifically down-regulated in MEFs were enriched for cell cycle–related processes, consistent with our previous report that the NSL complex is important for cell cycle progression in actively dividing cells (fig. S3, D and E) (*27*, *46*). The GO term intraciliary transport, along with other cilia-related terms, was enriched among the down-regulated genes shared between both cell types (fig. S3F). Finally, by plotting the differential expression data obtained in MEFs according to the gene order (dendrogram) generated through clustering of the podocyte expression data, it was revealed that genes within the GO term intraciliary transport are down-regulated in a similar manner in podocytes and MEFs (Fig. 2I). This down-regulation was not only evident at the RNA level, as we also found that the levels of several IFT proteins were markedly reduced in Kansl3-iKO MEFs (Fig. 2J and fig. S3G). In contrast to the loss of KANSL3 protein in Kansl2-pKO podocytes, KANSL2 protein was unaffected in Kansl3-iKO MEFs. Together, we concluded that while the NSL complex takes on an additional function in MEFs by regulating cell cycle–related genes, its core and conserved function in both dividing and postmitotic primary cell types is the transcriptional regulation of ciliary genes.

Transcriptional regulation of intraciliary transport genes is evolutionarily conserved between mouse and human

Cilia are essential components of almost all cells in the human body. Consequently, when ciliary function is impaired, it can affect various tissues and lead to diverse phenotypic outcomes, encompassing both isolated organ diseases and complex multisystem disorders (*43*, *47*). As the NSL complex components are conserved between mouse and human, we next wondered if the NSL complex–mediated transcriptional regulation of the intraciliary transport genes is also conserved. To this end, we obtained published RNA-seq data of KANSL2 knockdown (KANSL2-KD), KANSL3 knockdown (KANSL3-KD), and control human THP-1 cells from GSE158521 (*48*). We first compared the down-regulated genes between the published dataset and our podocyte dataset and found a substantial overlap between the two datasets (Fig. 2, K and L), suggesting that the NSL complex targets are conserved between human and mouse. Most genes in the GO term intraciliary transport are again down-regulated in KANSL2-KD and KANSL3-KD THP-1 cells as compared to control (Fig. 2M). Proteomics data from KANSL2-KD THP-1 cell show that of the 19 detected proteins from the GO term intraciliary transport, 10 were significantly down-regulated at the protein level (Fig. 2N) (*48*). Finally, we performed small interfering RNA (siRNA)–mediated knockdown on human proximal tubule HK-2 cells, a cell line often used to study cilia components and ciliopathy proteins, and found a similar down-regulation of genes encoding for intraciliary transport components (Fig. 2O) (*49*–*51*). Together, we confirmed that the NSL complex–mediated transcriptional regulation of intraciliary transport genes is evolutionarily conserved between mouse and human.

NSL complex depletion causes disappearance of primary cilia in ciliated cells

Proper control of ciliary genes is particularly important in ciliated cell types, where cilia act as signaling hubs. Furthermore, mutations in genes affecting cilia functions cause ciliopathies (*43*, *47*). On the other hand, classical cilia-related genes have also been implicated in extraciliary functions, which are likely to be more prominent in nonciliated cells. The finding that the NSL complex regulates intraciliary transport genes irrespective of whether the cell type of interest is ciliated or not is interesting and calls for further investigation of the potential cilia-independent function of these gene products. Therefore, we decided to compare the functional outcome of this transcriptional regulation in ciliated versus nonciliated cells. MEFs have been used as a cell culture model to study the function of important ciliary genes on primary cilia (*52*–*54*). We wondered if the loss of the NSL complex would result in the loss of cilia or cilia-related functions in MEFs. We induced formation of cilia in Kansl2-iWT or Kansl2-iKO MEFs after 4OHT treatment. Strikingly, we observed a strong and significant difference in the percentage of ciliated cells (Fig. 3A and fig. S3H). As primary cilia play an important role in the activation of the shh signaling pathway in mammalian cells, we next wondered if this pathway would be abrogated in the Kansl2-iKO cells (*53*–*55*). Treatment with SAG, a shh pathway agonist, triggered up-regulation of shh targets *Gli1* and *Ptch1* in Kansl2-iWT MEFs but failed to elicit a response in Kansl2-iKO MEFs (Fig. 3B). Collectively, these experiments revealed that NSL complex–mediated transcriptional regulation of intraciliary transport genes is important for cilia assembly and cilia-dependent functions in MEFs.

Establishment of an antibody-based FACS protocol to culture primary podocytes

To further study the causative functions of NSL complex–mediated transcriptional changes in podocytes, we established a primary podocyte culture system. Published primary podocyte culture systems rely on genetic tagging of the podocyte lineage by crossing Nphs2-Cre with the mTmG reporter (*56*–*58*). Because of the early onset of the phenotype in our Kansl2-pKO mice, we attempted to isolate and culture primary podocytes from 1-week-old mice before the onset of the phenotypes described earlier. However, after 7 days in culture, we only observed a mild down-regulation of *Kansl2* in FACS-sorted GFP^+ cells instead of a complete KO (fig. S4A). This might be explained by low *Nphs2* expression in podocyte culture compared to podocytes in vivo, resulting in insufficient Cre expression for the complete excision of both *Kansl2* alleles in culture (*59*). To circumvent this issue, we developed an antibody-based strategy to isolate primary podocytes from mouse models in which expression of Cre would not be affected by placing the cells in culture. We enriched for glomeruli by differential sieving of kidneys dissected from 7- to 10-day-old Kansl2-iWT and Kansl2-iKO mice (fig. S4B). To distinguish between podocytes and potential contamination from parietal epithelial and remaining tubular cells, a FACS strategy for $Podoplanin^+$ and $Prominin1^-$ cells was established (fig. S4C). Podoplanin had previously been shown to be a cell surface marker useful for sorting of podocytes, while Prominin1 has previously been demonstrated to mark the parietal epithelial and tubular cells (*57*, *60*–*64*). $Podoplanin^+Prominin1^-$ cells showed >10-fold higher expression of *Wt1,* the master transcription factor of podocytes, than $Podoplanin^+Prominin1^+$ cells (fig. S4D). Furthermore, the FACS strategy strongly enriched for WT1-positive cells as validated by immunofluorescence (fig. S4, E and F).

Kansl2-iWT and Kansl2-iKO podocytes were subjected to 4OHT treatment for 4 days to induce *Kansl2* deletion. Similar to the podocytes isolated from Kansl2-pKO mice, analysis of cultured Kansl2-iKO podocytes showed decrease of both mRNA and protein levels of genes within the GO term intraciliary transport (fig. S5, A to C). This further verified that the regulation of these genes by the NSL complex in podocytes was cell intrinsic. In contrast, deletion of *Kansl2* in cultured podocytes had no effect on either the RNA or protein levels of WT1 (fig. S5, A to C), an important indication that the podocyte cell identity was maintained after induction of KO in culture.

NSL complex depletion causes alteration of microtubule dynamics in cultured podocytes

Mature podocytes have been shown to lack cilia and shh pathway response (*42*, *65*). We confirmed that the cultured podocytes similarly lacked cilia and SAG treatment could not elicit a shh pathway response (Fig. 3, C and D). While canonical IFT protein complexes form within the context of cilia, others have shown that some IFT proteins retain their interactions in an extraciliary context (*44*). Therefore, we wondered if these proteins work independently or cooperatively in nonciliated podocytes. Despite the absence of cilia, coimmunoprecipitation of IFT complex proteins, IFT81 and IFT57, shows that both can interact with each other as well as with IFT88, indicating that some of these proteins might still form complexes with each other outside of the context of cilia and perform extra-ciliary functions in podocytes (Fig. 3E).

As cytoskeletal proteins are critical in enabling podocytes to carry out their filtration function and their abrogation is linked to podocytopathy, we wondered if we could observe cytoskeletal defects upon *Kansl2* deletion (*29*, *35*). We first compared the tubulin and actin cytoskeleton networks in Kansl2-iWT and Kansl2-iKO cultured podocytes and observed no marked difference at steady state (fig. S5D). However, we observed a decrease of both K40-acetylation and detyrosination of α-tubulin upon Kansl2-iKO, indicating potential alteration in microtubule dynamics in these cells (Fig. 3F and fig. S5E). Since the microtubule cytoskeleton is the primary structural constituent of both cilia and podocyte primary processes, we reasoned that deregulation of intraciliary transport genes upon KANSL2 loss may affect microtubule dynamics and/or microtubule-based transport. TTC21B, also known as IFT139, an IFT complex member, has recently been shown to be critical for podocyte functions, and its mutation is implicated in human primary focal segmental glomerulosclerosis (FSGS) (*66*).

We next challenged the microtubule network of the cells by treatment with nocodazole, a microtubule depolymerization agent. Immunofluorescence revealed a delay in repolymerization of microtubules after the removal of nocodazole in Kansl2-iKO podocytes compared to controls (Fig. 3G and fig. S5F). Alteration of microtubule dynamics has previously been demonstrated to affect podocyte cell migration, which in turn has been linked to podocyte foot process effacement in vivo (*67*, *68*). In accord with this, we performed migration assays and observed a delay in cell migration by Kansl2-iKO podocytes (Fig. 3H and fig. S5G). Finally, using an albumin influx assay, we found that Kansl2-iKO showed greater albumin influx across the podocyte monolayer. This suggests a functional impairment of the podocyte filtration barrier in cultured

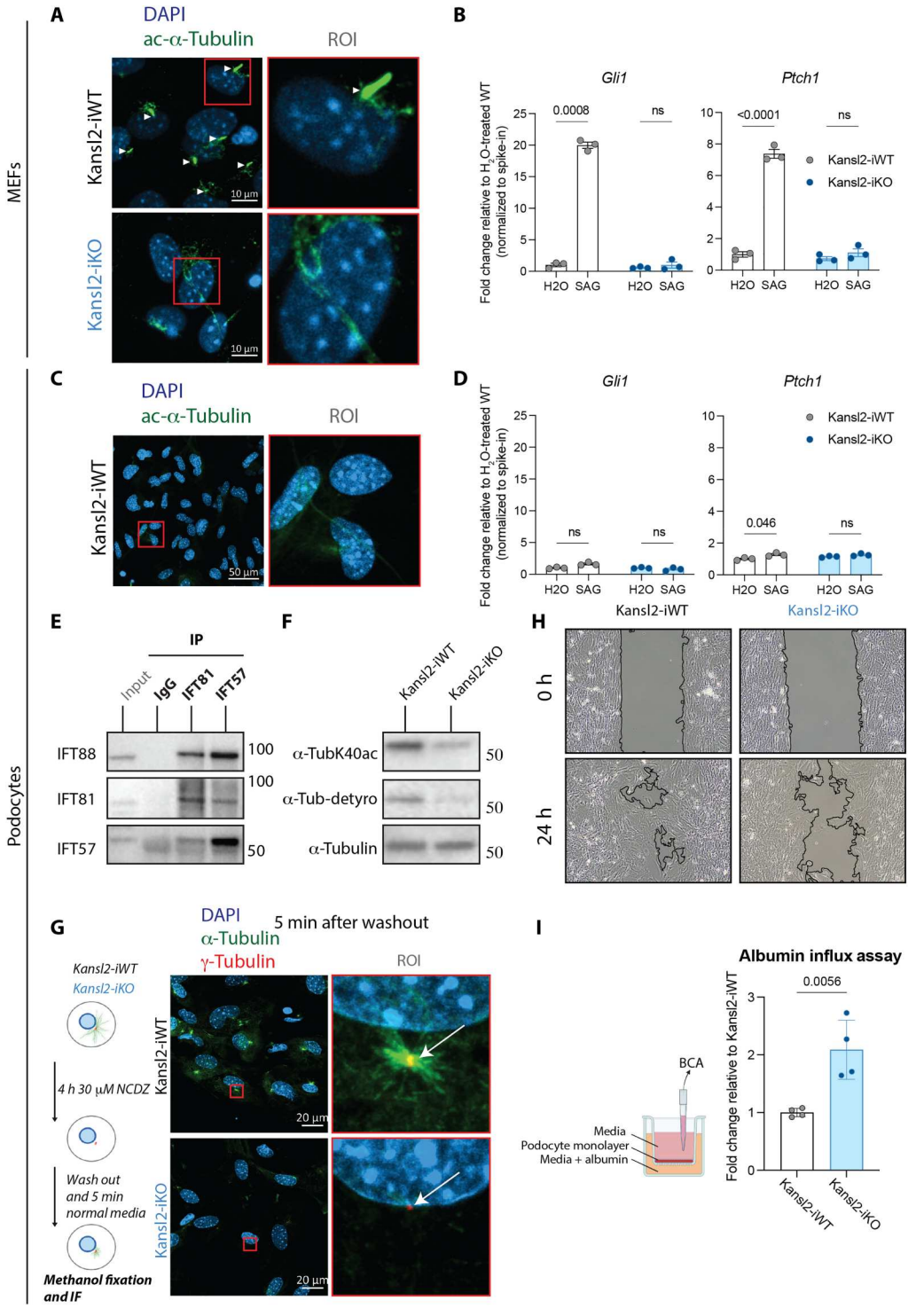

Fig. 3. Microtubule-related defects caused by KANSL2 depletion in ciliated and nonciliated cells. (**A**) Immunofluorescence of ac-α-tubulin as a readout of cilia in MEFs. Arrowheads point to cilia. See fig. S3H for quantification. (**B**) qRT-PCR of shh pathway genes in Kansl2-iWT and Kansl2-iKO MEFs (n = 3 per group). Data are presented as means ± SEM and were analyzed using two-way ANOVA followed by Tukey's multiple-comparison test. (**C**) Immunofluorescence of ac-α-tubulin in podocyte culture. No obvious cilia structures were observed. (**D**) qRT-PCR of shh pathway genes in Kansl2-iWT and Kansl2-iKO podocytes. SAG treatments failed to induce the shh response even in Kansl2-iWT podocytes (n = 3 per group). Data are presented as means ± SEM and were analyzed using two-way ANOVA followed by Tukey's multiple-comparison test. (**E**) Western blot showing immunoprecipitation of IFT81 and IFT57 in WT podocytes. (**F**) Western blot of tubulin modifications in Kansl2-iWT and Kansl2-iKO podocytes. See fig. S5E for quantification. (**G**) Experimental model (left) and immunofluorescence (right) of tubulin repolymerization assay after 5 min of recovery in Kansl2-iWT and Kansl2-iKO podocytes. (**H**) Migration assay of Kansl2-iWT and Kansl2-iKO podocytes. See fig. S5G for quantification. (**I**) Experimental model (left) and albumin influx assay (right) in Kansl2-iWT and Kansl2-iKO podocytes (n = 4 per group). Data are presented as means ± SEM and were analyzed using a two-tailed Student's t test.

Kansl2-iKO podocytes similar to that observed in vivo (Fig. 3I). Together, our primary podocyte culture data suggest that NSL complex–mediated transcriptional deregulation led to changes in microtubule dynamics and impaired functions in podocytes, molecular phenotypes that likely contributed to the emergence of podocytopathy in vivo.

The NSL complex directly regulates intraciliary transport genes via H4K5ac and H4K12ac

We next investigated if the deregulation of IFT genes was a direct consequence of NSL complex depletion in podocytes. To this end, we generated chromatin binding profiles of NSL members MOF and KANSL3 by chromatin immunoprecipitation sequencing (ChIP-seq) using the RELACS protocol in ex vivo WT podocytes

isolated as described in Fig. 2A (*69*). MOF and KANSL3 were strongly enriched around the promoter regions of commonly differentially down-regulated genes in both Kansl2-pKO and Kansl3-pKO as identified earlier in fig. S2D compared to a control group of random genes (Fig. 4A). This confirmed the direct regulation of most of these genes by the NSL complex. Similar enrichment was observed on genes in the GO term intraciliary transport when compared to the control group, indicating a direct involvement of NSL complex in the regulation of intraciliary transport genes (Fig. 4, B and C).

Although the NSL complex has been shown to acetylate H4K5ac, H4K8ac, H4K12ac, and H4K16ac in vitro, how the cellular context and cell identity influence target choice is not well understood (*12*, *13*, *48*). We wondered if the loss of NSL complex components led to a reduction in acetylation of these H4 residues in podocytes. We first performed Western blot and found no obvious bulk changes of either H4K5ac, H4K12ac, or H4K16ac when normalized to H4 level (fig. S5, H and I). This is expected, as H4K5ac and H4K12ac can be acetylated by other HATs, while H4K16ac is majorly mediated by MOF via the MSL complex (*22*, *48*, *70*–*74*). We reason that local changes of histone acetylations might not be reflected on the global level through Western blot. Therefore, we performed the first and most comprehensive analysis of H4 tail acetylation in ex vivo podocytes to date. Strikingly, Kansl2-pKO podocytes displayed significant loss of H4K5ac and H4K12ac at transcription start sites (TSS) of intraciliary transport genes (Fig. 4, D and E). In contrast, depletion of KANSL2 had no effect on H4K16ac levels at intraciliary transport genes in podocytes (Fig. 4F). These results agreed with studies showing that MOF catalyzes predominantly H4K5ac and H4K12ac through the NSL complex and H4K16ac primarily through the MSL complex (*13*, *48*). H3K9ac, a mark not deposited by the NSL complex, was unaffected by the loss of KANSL2 (Fig. 4G). Finally, histone marks associated with active promoters such as H3K4me3 and H3K27ac also showed a significant decrease at intraciliary transport genes upon loss of KANSL2, confirming that loss of H4K5ac and H4K12ac caused by KANSL2 depletion is accompanied by an altered chromatin landscape and transcription down-regulation of these genes (Fig. 4, H and I).

KANSL2 protects the integrity of the NSL complex

Despite its importance, the function of KANSL2 within the context of the NSL complex is not well defined. Our earlier findings that KANSL2 removal led to a stronger mouse phenotype than KANSL3 call for further investigation of its exact molecular function within the NSL complex. KANSL2 contains two uncharacterized double zinc finger (ZF-ZF) domains, a DLDV-containing domain that has been shown to interact with KANSL1 through WDR5 in vitro, and a putative mitochondria-targeting sequence in the N terminus (Fig. 5A) (*15*). We generated lentiviral-based overexpression constructs of KANSL2 and various KANSL2 mutants harboring deletion or replacement of some of these domains (Fig. 5A). To gain an understanding of which domains were the most important for the transcriptional regulation of intraciliary transport genes, we overexpressed these constructs in Kansl2-iKO podocytes and conducted quantitative reverse transcription polymerase chain reaction (qRT-PCR) analysis to see if the overexpression of the different KANSL2 constructs could rescue the transcriptional defects (Fig. 5, B and C, and fig. S6A). The WT KANSL2 construct rescued the transcriptional down-regulation of intraciliary transport genes, confirming that the NSL complex–mediated transcriptional defect resulting from *Kansl2* deletion was KANSL2 dependent (Fig. 5C). Furthermore, the WT KANSL2 construct restored H4K5ac and H4K12ac at the TSS of the intraciliary transport genes compared to a control group of random genes (Fig. 5, D and E). The transcriptional rescue of these genes is also reflected in the restoration of these components at the protein level (Fig. 5F, lanes 2 and 3, and fig. S6B). Constructs lacking either the N-terminal (ΔN) or C-terminal (ΔC) domains or in which the DLDV (ΔDLDV) or 1st ZF-ZF (Δ1st ZF) domains were replaced with a flexible linker show similar rescue activity as the WT KANSL2 construct, suggesting that each of these domains was dispensable for the transcriptional regulation function of the NSL complex at intraciliary transport genes (Fig. 5C). However, a KANSL2 mutant lacking the 2nd ZF-ZF domain (Δ2nd ZF) failed to rescue expression of *Ift* genes at both the RNA and protein levels (Fig. 5, C and F, lanes 2 and 4, and fig. S6B). Together, this identified the 2nd ZF-ZF domain as an important component of KANSL2 essential to NSL complex function.

Zinc fingers have previously been shown to act as mediators of protein-protein interactions, which can fine-tune functions of chromatin-modifying complexes including HAT complexes (*75*). The 2nd ZF-ZF of KANSL2 represents a previously uncharacterized class of zinc finger and is evolutionarily conserved. It shares similarity with the ZF-ZF of INO80D, member of the INO80 chromatin-modifying complex, which has previously been shown to interact with the NSL complex (*12*, *45*). We therefore wondered if the 2nd ZF-ZF could be a mediator of protein-protein interaction. We discovered that the KANSL2-Δ2nd ZF mutant failed to interact with the rest of the NSL complex proteins, suggesting the importance of its presence in mediating interaction between KANSL2 and the NSL complex (Fig. 5G). Loss of KANSL2 led to reduced protein levels of other NSL complex members, although they were transcriptionally unaffected (Fig. 5H, fig. S6C, and table S1). This suggests that the loss of KANSL2 destabilized the rest of the NSL complex. Overexpression of WT KANSL2 could partially rescue the protein expression of the NSL complex members, while the KANSL2-Δ2nd ZF mutant failed to do so, further verifying the importance of the 2nd ZF-ZF domain in NSL complex stability (Fig. 5I and fig. S6D). Zinc fingers are also well known for their DNA binding property, while it was not clear if KANSL2 had DNA binding ability. We therefore purified MBP-KANSL2-3×Flag and conducted electromobility shift assay with MBP-KANSL3-3×Flag and MBP-3×Flag acting as positive and negative controls, respectively (fig. S6, E and F) (*18*). We found no evidence of DNA binding for KANSL2 in our in vitro assay. This further confirmed that the primary function of the 2nd ZF-ZF domain is protein-protein interaction. Finally, the alterations in tubulin posttranslational modification state caused by KANSL2 deletion can also be partially rescued by ectopic expression of the WT but not KANSL2-Δ2nd ZF, consistent with the transcriptional rescue of IFT genes and proteins (Fig. 5J and fig. S6G). Together, we provided initial characterization of a previously undescribed zinc finger domain and our results pointed to the importance of the 2nd ZF-ZF domain of KANSL2 in mediating its interaction with the rest of the NSL complex. The loss of this interaction caused instability of the NSL complex and rendered it dysfunctional, leading to transcriptional deregulation and the phenotypic manifestation observed in podocytes.

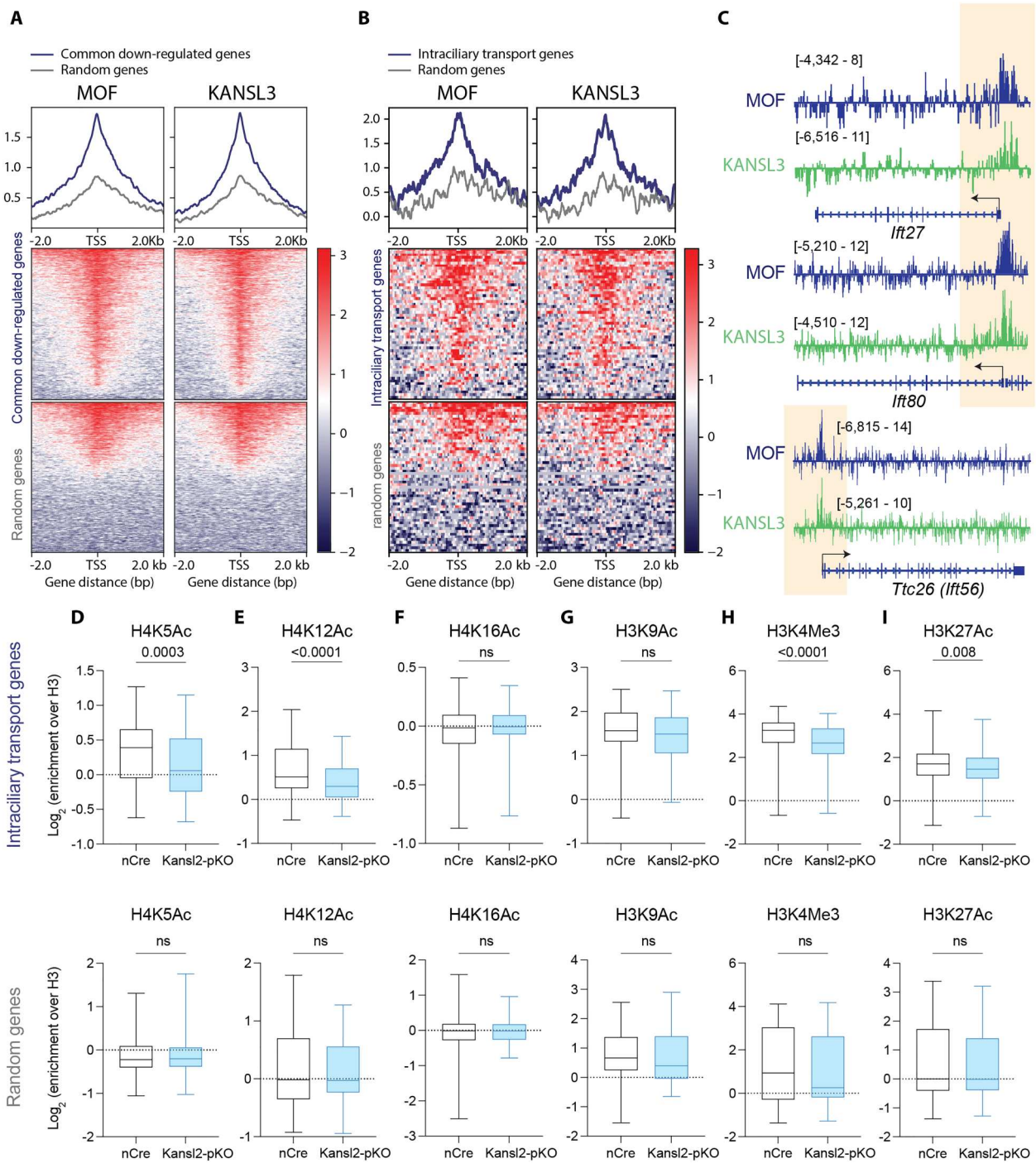

Fig. 4. *Ift* genes are direct target of NSL complex and show loss of H4K5 and H4K12 acetylations upon KANSL2 depletion. (**A**) Metagene profile (top) and heatmap (bottom) showing TSS binding of MOF and KANSL3 at a group of commonly down-regulated genes in both Kansl2-pKO and Kansl3-pKO ($n = 1585$) versus a control group of randomly selected genes ($n = 1582$). (**B**) Metagene profile (top) and heatmap (bottom) showing TSS binding of MOF and KANSL3 at genes in the GO term intraciliary transport ($n = 55$) versus a control group of random genes ($n = 55$). (**C**) IGV snapshot of MOF and KANSL3 binding at TSS of *Ift* genes. (**D** to **I**) Box plots showing enrichment of H4K5ac (D), H4K12ac (E), H4K16ac (F), H3K9ac (G), H3K4me3 (H), and H3K27ac (I) at intraciliary transport genes ($n = 55$) (top) versus a control group of random genes ($n = 55$) (bottom) in nCre and Kansl2-pKO podocytes. ChIP signals of individual histone modifications were normalized to H3 (data are presented as minimum to maximum and were analyzed using a two-tailed Student's *t* test).

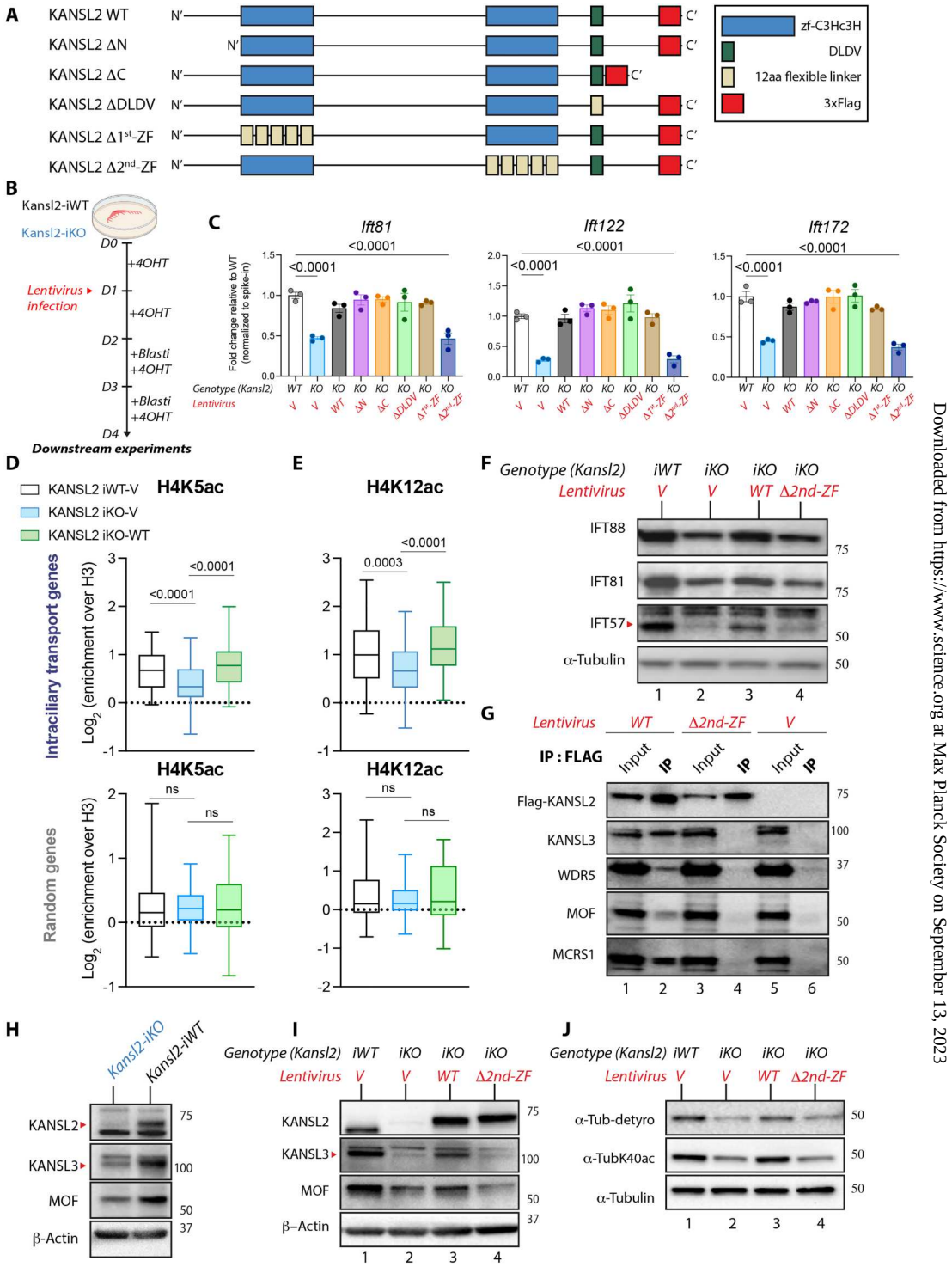

Fig. 5. The second zinc finger of KANSL2 is required for NSL-mediated transcriptional regulation of intraciliary transport genes. (**A**) Constructs used for lentivirus-based overexpression experiments. (**B**) Schematic of lentivirus-based overexpression experiments. (**C**) qRT-PCR of *Ift* genes in podocytes with the indicated genotypes and overexpression constructs ($n = 3$ per group). Data are presented as means ± SEM and were analyzed using the ordinary one-way ANOVA followed by Tukey's multiple-comparison test. (**D** and **E**) Box plots showing enrichment of H4K5ac (D) and H4K12ac (E) at intraciliary transport genes ($n = 55$) (top) versus a control group of random genes ($n = 55$) (bottom) in MEFs with the indicated genotype and lentiviral constructs. ChIP signals of individual histone modifications were normalized to H3 (data are presented as minimum to maximum and were analyzed using the ordinary one-way ANOVA followed by Tukey's multiple-comparison test.) (**F**) Western blot of IFT proteins in podocytes with the indicated genotypes and overexpression constructs. See fig. S6B for quantification. (**G**) Immunoprecipitation of FLAG in nuclear extract of WT podocytes with the indicated overexpression constructs. The KANSL2-Δ2nd ZF mutant failed to bind to the other NSL complex members. (**H**) Western blot of NSL complex proteins in WT and Kansl2-iKO podocytes. See fig. S6C for quantification. (**I**) Western blot of the NSL complex proteins in podocytes with the indicated genotypes and overexpression constructs. See fig. S6D for quantification. (**J**) Western blot of tubulin modifications in podocytes with the indicated genotypes and overexpression constructs. See fig. S6G for quantification.

DISCUSSION

Proteins adapt to changes of cellular environment and perform different functions depending on the cellular context and localization. For example, we have previously reported that NSL complex members with known roles in transcriptional regulation in the nucleus also localize to mitochondria or the mitotic spindle to perform compartment-specific functions (*13*, *36*). Here, we provide evidence that transcriptional regulation of ciliary gene networks is an evolutionarily conserved and core function of the NSL complex. Misregulation of these genes, as a result of depletion of the NSL complex members, led to diverse outcomes in different cell types (Fig. 6, model). In ciliated MEFs, dysfunction of the NSL complex led to the loss of cilia and shh pathway, whereas in non-ciliated podocytes changes in microtubule dynamics and

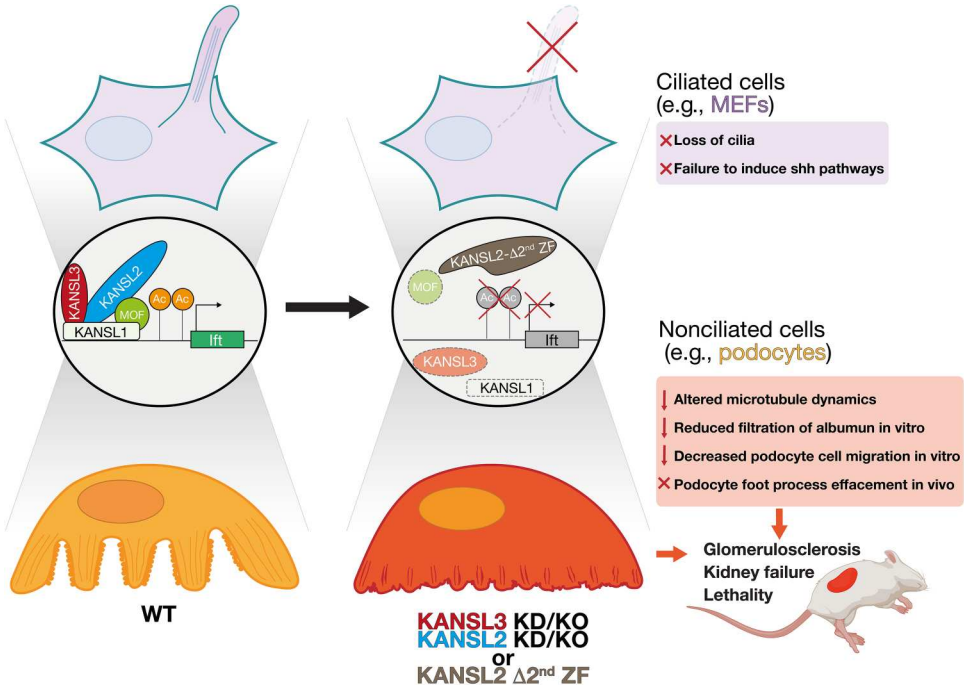

Fig. 6. NSL complex–mediated regulation of *Ift* genes exhibits a bifurcation of functions to enable diversity of specialized outcomes in two differentiated cell types. The evolutionary conserved NSL complex mediates transcriptional regulation of *Ift* genes via histone acetylations in both mouse and human cells. Depletion of the NSL complex members KANSL2 or KANSL3, or expression of the KANSL2-Δ2nd ZF mutant, results in the loss of *Ift* gene expression. In ciliated cells, this leads to the loss of cilia and the failure to induce shh pathways, while in nonciliated cells such as podocytes, this leads to altered microtubule dynamics, reduced albumin filtration and decreased cell migration in vitro, as well as podocyte foot process effacement in vivo. Mice with podocyte-specific deletion of *Kansl2* or *Kansl3* suffer from glomerulosclerosis and kidney failure, eventually leading to early lethality.

microtubule-related functions were observed. In vivo podocyte-specific deletion of *Kansl2* and *Kansl3* led to severe glomerulosclerosis, eventually resulting in lethality. Given the demonstrated influence of *Ift* genes on microtubule dynamics and cell migration in nonciliated cells (see later in Discussion) and the indispensability of a properly organized microtubule cytoskeleton to the integrity of podocyte foot processes, we hypothesize that aberrant microtubule dynamics represent the most likely cause of the podocytopathy observed upon the loss of NSL complex proteins in vivo. While KANSL3 is capable of directly associating with microtubules during mitosis, here we show that in postmitotic cells KANSL2 and KANSL3 regulate microtubule stability through transcriptional regulation of microtubule-associated proteins. The NSL complex therefore regulates microtubule functions via two completely different mechanisms in mitotic versus interphase cells and is yet another example of how proteins diversify their functions depending on cellular status.

Our study reveals a critical role for intraciliary transport proteins in nonciliated cells, a theme that has received relatively little attention. It came as a surprise when a missense mutation of the *TTC21B* (also known as *IFT139*) gene was identified in seven families with FSGS (*66*). However, the authors could confirm that the IFT139 protein was expressed in terminally differentiated podocytes despite their unciliated status and could additionally show that IFT139 changes its localization from the base of the primary cilium in immature podocytes during early nephron development to the extended microtubule network in fully differentiated nonciliated podocytes. Knockdown or the expression of a mutant form of IFT139 in podocytes led to microtubule organization defects, confirming a function of IFT139 in podocytes outside of the cilia context (*66*). Another study providing evidence that IFT proteins have functions outside of cilia established IFT88 as a centrosomal protein regulating G_1-S transition in nonciliated, actively dividing HeLa cells (*76*). Other studies have discovered that certain IFT proteins can have very specialized cell type–specific functions, such as the formation of the immune synapse in T cells, or in vesicular transport for postsynaptic dendrites in neurons (*44*, *77*). The microtubule repolymerization defects observed in Kansl2-iKO podocytes in the current study were also previously observed in *Ift52*-deleted cells, confirming that transcriptional down-regulation of *Ift52* has the capacity to produce marked changes in microtubule dynamics (*78*). Furthermore, knockdown of IFT139 in podocytes has been previously shown to lead to a decrease in cell migration, consistent with the Kansl2-iKO phenotype observed in the current study (*66*). The present study is therefore consistent with a growing body of literature pointing to the relevance of IFT proteins in nonciliated cells such as podocytes. While other studies focused on individual *Ift* genes, our work identified the NSL complex as a major transcriptional regulator of these genes via H4 tail acetylation. In a series of molecular events, the concerted loss of functions of the IFT proteins translate into effects on microtubule cytoskeleton-based phenotypes in nonciliated cells.

We have shown here that the transcriptional regulation of intraciliary transport genes by the NSL complex is evolutionary conserved from human to mouse. Therefore, the observation that the loss of KANSL2 or KANSL3 results in podocyte foot process

effacement may warrant further investigation of these proteins in the context of human kidney diseases. In addition, the current finding that the NSL complex mediates transcriptional regulation of *Ift* genes in ciliated cells has substantial implications in human disease contexts where cilia or cilia-dependent signaling pathways play important roles. For example, members of the NSL complex have been shown to be misregulated in different types of cancers (*11*, *45*, *79*, *80*). We show here that dysfunction of the NSL complex causes loss of cilia and shh response, which makes it plausible to expect that the deregulation or mutation of NSL proteins in these cancers could drive shh-dependent phenotypic changes. Consistent with this, while shh is known to facilitate cancer invasion in the context of metastasis, KO of KANSL2 in cancer cells has been shown to significantly impair cancer cell invasion (*81*, *82*). In addition, human mutations of *MOF* and *KANSL1* have been associated with multiorgan developmental syndromes (*4*, *8*). Notably, patients suffering from Koolen–de Vries syndrome (*KANSL1* haploinsufficiency disorder) have developmental problems and symptoms including septal heart defects, hydronephrosis, or duplex renal system, all of which has previously been associated with the shh pathways and the latter has also been shown in mice carrying *Ift25* and *Ift27* null mutants (*83*–*86*). Our discovery that the NSL complex is important for cilia-related gene expression could help us better understand the pathogenesis of these disorders and is an important path to pursue in the future.

Studies and resources on the role of epigenetic modulators in podocytes are relatively limited compared to other cell types (*87*, *88*). This might be partially due to the notorious difficulty to both isolate and culture podocytes, a challenge that is further hampered by the naturally limited number of podocytes in animal models (*89*). As a result, it is difficult to conduct molecular analysis such as ChIP where large amounts of input materials are required for traditional methods. We provided here, to our knowledge, the first genome-wide profiles for multiple histone modifications in podocytes directly isolated from mice. This includes traditional promoter and enhancer markers H3K4me3 and H3K27ac, as well as the NSL complex–related histone marks H4K5ac, H4K12ac, and H4K16ac. These profiles will be valuable for the nephrology community beyond the current study. Other HATs and their related complexes, such as the NuA4/TIP60 complex, have also been shown to acetylate H4K5, H4K12, and H4K16 in vitro (*10*, *70*, *72*, *73*). However, in vivo evidence showing that TIP60 is a major HAT for the aforementioned acetylations is rather limited. For example, TIP60 deletion in Drosophila KC cells or in MEFs has no effect at either of these acetylation sites, indicating that other HATs are also contributing to acetylation at these sites (*71*, *90*). Nevertheless, further studies on HATs in the context of podocytes should be conducted. Finally, we provided here first ex vivo evidence of H4K12ac loss upon the deletion of NSL complex member KANSL2, thus confirming previous in vitro findings (*13*, *21*).

Apart from an earlier study demonstrating the involvement of the KANSL2 DLDV domain in mediating interaction with fellow NSL complex member WDR5, the function of the other predicted structural domains in KANSL2 have not been characterized (*15*). We provide evidence that KANSL2 itself is important for the integrity as well as the function of the NSL complex, and the 2nd ZF-ZF domain of KANSL2 plays an important role in mediating its interaction with the rest of the NSL complex members. The 2nd ZF-ZF domain is highly conserved among species and is structurally similar to the ZF-ZF domain of INO80D. KANSL2 has been identified as an interaction partner of INO80E in a mass spectrometry–based analysis in human cells (*91*). The importance of this interaction and whether the interaction is mediated by the 2nd ZF-ZF of KANSL2 should be further investigated in the future.

MATERIALS AND METHODS

Animals

All animal studies and experimental procedures were performed according to the German animal care and ethics legislation and were approved by the local government authority, the Committee on Research Animal Care, Regierungspräsidium Freiburg (G-18/144). The study is compliant with all relevant ethical regulations regarding animal research. The *Kansl2*-floxed, *Kansl3*-floxed, and *Nphs2-Cre* mouse strains have been previously described (*26*, *27*). The *Cag-Cre-ERT2* and Gt(ROSA)26Sor$^{tm4(ACTB-tdTomato,-EGFP)Luo/J}$ (referred to as *mT/mG*) mice were purchased from The Jackson Laboratory (Bar Harbor, ME, USA). All mice were maintained on a C57BL/6 background and kept under a 14-hour light and 10-hour dark cycle, and water and standard chow were available ad libitum. Genotyping was undertaken through standard PCR using the primers listed in table S5.

Albumin:creatinine ratio

Urine was collected once a week from week 1 to week 6. Urinary albumin and creatinine were measured using the BCG Albumin Assay Kit (Sigma, MAK124) and Creatinine (urinary) Colorimetric Assay Kit (Cayman, 500701), respectively, according to the manufacturer's instructions.

Histology

Kidneys from 6-week-old Kansl2-pKO, Kansl3-pKO, and nCre control mice were dissected, fixed in 4% paraformaldehyde (PFA) in phosphate-buffered saline (PBS), dehydrated, and embedded in paraffin. Sections (4 μm) were cut on a Leica microtome before being further processed for PAS or Sirius red staining. The images were captured with an Axioimager Apotome microscope using Axiocam MRc color charge-coupled device (CCD) camera (Carl Zeiss) and analyzed with the Axiovision software (Carl Zeiss) for Axioimager Apotome.

Electron microscopy

For ultrastructural analysis by TEM, kidneys were fixed in 4% PFA and 2% glutaraldehyde (Carl Roth, #4157) in 0.1 M cacodylate buffer (Science Services, #11650). Samples were postfixed in 0.5% osmium tetroxide (Science Services, #E19150) in double-distilled water (ddH_2O) for 60 min on ice and then washed six times in ddH_2O. The tissue was stained en bloc in 1% uranyl acetate solution (Science Services, #E22400-1) for 2 hours in the dark and washed two times in ddH_2O. Dehydration was performed by sequential 15-min incubation steps in 30%, 50%, 70%, 90%, and 2× 100% ethanol (Fisher Scientific, #32205) and then 2× 100% acetone (Sigma-Aldrich, #179124). After embedding in Durcupan resin (Sigma-Aldrich, #44611 and #44612), ultrathin sections (55 nm) were performed using a UC7 ultramicrotome (Leica), collected on Formvar-coated (Science Services, #E15830-25) copper grids (Plano, #G2500C). Poststaining was done for 1 min with 3% lead citrate (Delta Microscopies, #11300). For SEM, the fixated samples were

dehydrated in 70%, 80%, 90%, and 100% ethanol (each step for 1 hour at room temperature) and incubated in a 1:1 solution of ethanol and hexamethyldisilazane (HMDS; Carl Roth, #3840.2) for 30 min. After incubation in 100% HMDS, the solvent was allowed to evaporate. The dehydrated tissue was mounted onto sample holders and sputtered with gold using Polaron Cool Sputter Coater E 5100 (*92*). Quantification of foot process effacement was done by counting slit diaphragms in TEM micrographs and setting the resulting numbers in relation to the length of the basement membrane, resulting in a SD/µm. In total, four different glomeruli per mouse were analyzed, and for each genotype, three mice were analyzed.

Ex vivo isolation of podocytes

Podocytes were isolated as described previously with modifications (*37*). In brief, Kansl2-pKO, Kansl3-pKO, and nCre mice were further crossed with mTmG mice to genetically label podocytes with enhanced GFP (eGFP) (Fig. 1A). Three-week-old mice were sacrificed, and their kidneys were dissected and minced. They were then incubated in digestion solution for 15 min at 37°C [collagenase II (300 U/ml) (Worthington), pronase E (1 mg/ml) (Sigma), and deoxyribonuclease (DNase) I (50 U/µl) (Applichem) in Hanks′ balanced salt solution (HBSS)]. The digestion solution was then passed through 100-µm sieves twice, washed with HBSS, and spun down. The pellets were resuspended and incubated again in digestion solution for 40 min at 37°C. The digested solution was again spun down and resuspended in Buffer ACK (Gibco, A1049201) on ice for the lysis of red blood cells. After 5 min of incubation, the resulting solution was spun down. The single cells were resuspended in FACS buffer (0.2% FCS and 2 µM EDTA in PBS) supplemented with 1:500 Zombie-NIR (BioLegend, 423105). For DNA, RNA, or protein analysis, the cells were then passed through a 35-µm cell strainer. GFP-positive cells were FACS-sorted on a FACS MoFlo flow cytometer into ice-cold PBS supplemented with 2% FCS. For ChIP, after 10 min of Zombie-NIR staining, the cells were spun down and fixed in 1% PFA for 10 min at room temperature. The fixed cells were then spun down, resuspended in FACS buffer, and passed through a 35-µm cell strainer. GFP-positive cells were FACS-sorted on a FACS MoFlo flow cytometer into ice-cold PBS. The cells were then pelleted by centrifugation (1500 rpm, 5 min, 4°C), and the pellets were snap-frozen and stored at −80°C.

MEF culture

MEFs were cultured from embryonic day 13.5 *Kansl2*$^{fl/fl}$, *Kansl2*$^{fl/fl}$ *Cag-Cre-ERT2*$^{T/+}$, *Kansl3*$^{fl/fl}$, and *Kansl3*$^{fl/fl}$ *Cag-Cre-ERT2*$^{T/+}$ embryos as described previously (*27*). MEFs were maintained in Dulbecco′s modified Eagle′s medium (Gibco, 11960-044) supplemented with penicillin (100 U/ml) and streptomycin (100 µg/ml) (Sigma, P4333), 1 mM sodium pyruvate (Gibco, 11360-039), 1× GlutaMAX (Gibco, 35050-038), and 10% fetal calf serum (FCS). To induce *Kansl2* or *Kansl3* deletion, MEFs were cultured in the presence of 2 µM 4OHT (Sigma, SML1666) for 4 days. For the induction of cilia, cells were cultured in reduced medium (0.25% FCS) for 24 hours 3 days after the start of 4OHT treatment. For SAG treatment, cells were treated with 200 nM of the shh pathway agonist SAG (Merck, 566661) in reduced medium (0.25% FCS) for 24 hours 3 days after the start of 4OHT treatment.

Primary podocyte cell culture

Seven- to 10-day-old *Kansl2*$^{fl/fl}$ *Cag-Cre-ERT2*$^{T/+}$ and littermate control mice were sacrificed, and their kidneys were dissected and minced. They were then incubated in digestion solution for 12 min at 37°C [collagenase II (300 U/ml) (Worthington), pronase E (1 mg/ml) (Sigma), and DNase I (50 U/µl) (Applichem) in HBSS]. The digestion solution was then passed through sieves with decreasing pore sizes (100, 70, and 40 µm), washed with HBSS, and spun down. The glomeruli were resuspended in complete medium [RPMI 1640 supplemented with penicillin (100 U/ml) and streptomycin (100 µg/ml) (Sigma, P4333), 1× GlutaMAX (Gibco, 35050-038), insulin-transferrin-selenium (10 ml/liter) (Corning, 25-800-CR), and 10% FCS]. The cells were cultured at 37°C and 5% CO_2 for 7 days. After 7 days, glomerular cells were FACS-sorted for Podoplanin-PE (phycoerythrin)–positive, Prominin1-APC (allophycocyanin)–negative, and Zombie-NIR–negative live cells (tables S7 and S8) and plated for downstream experiments. To induce *Kansl2* or *Kansl3* deletion, podocytes were cultured in the presence of 2 µM 4OHT for 4 days. For the induction of cilia, cells were cultured in reduced medium (0.25% FCS) for 24 hours 3 days after the start of 4OHT treatment. For SAG treatment, cells were treated with 200 nM of the shh pathway agonist SAG (Merck, 566661) in reduced medium (0.25% FCS) for 24 hours 3 days after the start of 4OHT treatment.

siRNA-mediated knockdown in human proximal tubule cell line HK-2 cells

HK-2 cells were cultured in Dulbecco′s Modified Eagle′s Medium/Nutrient Mixture F-12 (DMEM)/F12 (Gibco, 11330-032) supplemented with penicillin (100 U/ml) and streptomycin (100 µg/ml) (Sigma, P4333), 1 mM sodium pyruvate (Gibco, 11360-039), insulin-transferrin-selenium (10 ml/liter) (Corning, 25-800-CR), 5% FCS, and human epidermal growth factor (5 ng/ml) (STEMCELL Technologies, #78136). siRNA (10 nM) against human KANSL2 (Sigma-Aldrich, SASI_Hs01_00247424) or Silencer Negative Control No. 2 (Thermo Fisher Scientific, AM4613) was transfected using Lipofectamine RNAiMAX (Invitrogen, 13778-100) according to the manufacturer′s protocol.

Microtubule repolymerization assay

Podocytes were plated on eight-well imaging chambers after FACS. Four days after 4OHT treatment, cells were treated with 30 µM nocodazole (Abcam, 120630) for 4 hours at 37°C. Cells were then washed with PBS, incubated at 37°C for 5 or 15 min, and then fixed in −20°C 100% methanol for 10 min. Immunofluorescence was carried out as described.

Migration assay

Podocytes were plated on two-well culture insert (ibidi, 81176) after FACS. Four days after 4OHT treatment, a scratch was performed by removing the culture insert. Image was captured at 0 and 24 hours with a conventional CCD camera on a regular inverted cell culture microscope with a 10× objective. Images were analyzed by the ImageJ plugin "Wound healing size tool" (*93*).

Albumin flux assay

The permeability of the podocyte monolayer to albumin was measured as previously described (*94*). Briefly, podocytes were seeded in the upper chambers of 3-µm polycarbonate Transwell filters of a 24-

well filtration microplate (Corning). Four days after 4OHT treatment, cells were washed with PBS supplemented with 1 mM $MgCl_2$ and 1 mM $CaCl_2$ to protect the cadherin-based junctions. The top chamber was filled with 0.15 ml of complete medium, and the bottom chamber was filled with 750 μl of complete medium supplemented with bovine serum albumin (BSA; 40 mg/ml). Two hours later, the medium from the upper chamber was collected, and the albumin concentration was measured using the Pierce Rapid Gold BCA Protein Assay Kit (Thermo Fisher Scientific, A53225).

Lentivirus-mediated ectopic expression

WT FLAG-tagged KANSL2 as well as various KANSL2 mutants (Fig. 5A) were cloned into the pCHDblast MCSNard plasmid (Addgene vector no. 22661) using the Xba I and Not I cloning sites. The "negative vector" contained a 22–base pair (bp) fragment inserted into the same vector but lacked an open reading frame. This vector contains a cytomegalovirus (CMV) promoter and a blasticidin selection marker. Lentivirus was produced as previously described, and MEFs or podocytes were infected 1 day after the start of 4OHT treatment (*22*). Selection began 24 hours after infection and was carried out over 2 days using blasticidin-HCl (2 μg/ml) (Gibco, A11139-03).

Quantitative RT-PCR

For qRT-PCR analyses, RNA was extracted from ex vivo isolated podocytes or cultured podocytes using the Quick-RNA Microprep Kit (Zymo, R1051). For MEFs, RNA was extracted using the Quick-RNA Miniprep Kit (Zymo, R1055). Reverse transcription reactions were carried out using the GoScript Reverse Transcriptase (Promega, A5001) as per the manufacturer′s instructions. In some experiments, Drosophila S2 cells RNA were added into the reverse transcription reaction as spike-in. The transcript levels were quantified using SYBR green chemistry on an LC480 instrument (Roche). The primer sequences are provided in table S6.

Protein expression and purification

6His-MBP-hKANSL3-3xFlag, 6His-MBP-mKANSL2-3xFlag, and 6His-MBP-3xFlag control were expressed in the insect cell line SF21 using the Invitrogen Bac-to-Bac system. Actively dividing SF21 cells were transfected with gene constructs containing the respective expression constructs. The cells were incubated at 27°C in SF900 II-medium without serum and antibiotic for 72 hours. After 72 hours, the supernatant was collected as virus P0, which was then used to infect SF21 cells again. Forty-eight to 72 hours after infection, the cells were harvested and virus P1-stock was collected. After the last round of virus amplification, virus P2-stock was used to infect 50 million cells of SF21. After 48 hours, cells were collected and the pellet was lysed in HMG 150 buffer [25 mM Hepes (pH 7.6), 12.5 mM $MgCl_2$, 10% glycerol, and 150 mM KCl] supplemented with 0.2% NP-40 and Complete Protease Inhibitor (Roche). Whole-cell extract was obtained using a Dounce homogenizer with a tight pestle. After centrifugation at 4000 rpm at 4°C for 45 min, prewashed Flag M2 agarose gel (Sigma, A2220) was added to the extract and incubated for 2 hours at 4°C on a rotating wheel. The Flag-beads were washed three times with the HMG 150 buffer, and elution was performed with 3×Flag-peptide (300 μg/ml) (Sigma, F4799) in the same buffer for 1 hour at 4°C on a rotating wheel. A fraction of the eluate was loaded on a Coomassie blue–stained polyacrylamide gel electrophoresis (PAGE) gel to check protein quantity and quality. The eluate was snap-frozen in liquid nitrogen and stored at −80°C for later use.

Electromobility shift assay

Cy3-labeled luciferase double-stranded DNA (dsDNA) was amplified from a firefly luciferase–containing plasmid using the Cy3-labeled forward primer 5′-[Cy3]-TGCCTAAAGGTGTCGCTCTG-3′ and the unlabeled reverse primer 5′-TCATCCCCCTCGGGTGTAAT-3′. dsDNA (100 fmol) was mixed with increasing amounts of purified proteins. The reaction was conducted in 1× Assay Buffer [50 mM tris-HCl (pH 8), 5% glycerol, 150 mM KCl, and BSA (0.1 mg/ml)] for 30 min on ice. The samples were then diluted with 6× Orange DNA Loading Dye (Thermo Fisher Scientific, R0631) and loaded on a 2% agarose gel. The images were developed using Typhoon FLA 9500 (GE Healthcare) with the Cy3 channel at 900 V.

Immunofluorescence

Cells were fixed and permeabilized by either 100% methanol for 10 min at −20°C or 4% PFA in PBS for 10 min at room temperature followed by 0.3% Triton X-100 in PBS for 10 min at room temperature. Blocking was performed by incubation in 0.25% gelatine in PBS for 1 hour at room temperature. The cells were then incubated with the appropriate primary antibodies overnight at 4°C. After three washes with PBS for 5 min at room temperature, cells were incubated with appropriate secondary Alexa Fluor–conjugated antibodies (table S7). For actin staining, Alexa Fluor 647 Phalloidin (CST 8940s) was used together with the secondary antibodies (table S8). The cells were then counterstained and mounted with VECTASHIELD PLUS Antifade Mounting Medium with DAPI (4′,6-diamidino-2-phenylindole (Vector Laboratories, H-2000). The images were captured with an LSM900 microscope equipped with an Airyscan2 detector (Carl Zeiss) and analyzed with the Zen Blue software (Carl Zeiss).

Cellular fractionation

Cell fractionation was undertaken using Subcellular Protein Fractionation Kit for Cultured Cells (Thermo Fisher Scientific, 78840) as per the manufacturer′s instructions (*26*).

Immunoprecipitation

Immunoprecipitation assays were carried out on cell lysates prepared in HMG150 buffer [25 nM Hepes (pH 7.6), 12.5 mM $MgCl_2$, 10% glycerol, 150 mM KCl, 0.5% Tween 20, and Protease Inhibitor cOmplete Mini (Roche, 04693159001)]. For Flag-based immunoprecipitation, each Flag immunoprecipitation was performed with 100 μg of proteins and the Anti-Flag M2 Magnetic Beads (Millipore, M8823) as per the manufacturer′s instructions. Eluted samples were used for Western blot analysis. For antibody-based immunoprecipitation, a 1:1 ratio of Sepharose protein A: protein G beads (GE Healthcare, 17-5280-02 and 17-0618-05) blocked with BSA (0.2 mg/ml) was used to preclear the cellular lysates. Each immunoprecipitation was performed on 200 μg of protein with 5 μg of IFT57, IFT81, or rabbit immunoglobulin G (IgG) antibodies (table S7) overnight at 4°C. Following the immunoprecipitation, 100 μl of blocked protein A/G beads was added and the mix was incubated for 1 hour at 4°C on a rotating wheel. The mix was then washed three times in HMG150 (10 min each), and

elution was performed by incubation in 50 μl of ROTI-load (Roth, K929.1) for 5 min at 95°C. The eluted samples were then spun down, and the supernatant was used for Western blot analysis.

Western blot

Western blot analyses were performed using standard methods. Briefly, 10 to 20 μg of whole-cell lysates or 5 to 10 μg of cellular fractions were run on a 4 to 12% gradient gel (Thermo Fisher Scientific) and proteins were transferred to a polyvinylidene difluoride (PVDF) membrane (Amersham, 10600021). The membrane was blocked in 5% skim milk and incubated overnight with the appropriate primary antibody (table S7). After washing, the membrane was incubated with the appropriate secondary horseradish peroxidase (HRP)–conjugated antibody (table S7) and developed using the Lumi-Light reagent (Roche, 12015200001) with detection of chemiluminescence on a Bio-Rad Chemidoc XRS+ instrument. Quantification and image analyses were carried out using the Image Lab software (v5.2, Bio-Rad Laboratories) (*26*).

RNA sequencing

Ex vivo isolated podocytes

Podocytes were FACS-sorted as described earlier. To ensure consistency and eliminate batch effect, RNA extractions were performed simultaneously for all samples using the Quick-RNA Microprep Kit (Zymo, R1051). The RNA quality was examined using the 5200 Fragment Analyzer (Agilent). Libraries were prepared using the NEBNext Single Cell/Low Input RNA Library Prep Kit for Illumina (NEB, E6420) and sequenced on the NovaSeq 6000 instrument (Illumina). Each condition was performed with four biological replicates. Data processing, quality control, trimming, and mapping were performed using snakePipes mRNA-seq pipeline (*95*). Differential expression analysis was performed using DESeq2 with a false discovery rate (FDR) cutoff of 0.05 (*96*). GSEA and overrepresentation analysis were performed using the ClusterProfiler package in R (*97*). Heatmaps of *z* score were generated using the pheatmap package in R.

Mouse embryonic fibroblasts

WT and KO MEFs following 4 days of tamoxifen treatment were directly lysed on plate with 300 μl of TRIzol (Thermo Fisher Scientific, 15596018). To ensure consistency and eliminate batch effect, RNA extractions were performed simultaneously for all samples using the Quick-RNA Miniprep Kit (Zymo, R1055). The RNA quality was examined using the 5200 Fragment Analyzer (Agilent). Libraries were prepared using TruSeq Stranded Total RNA Library Prep Gold (Illumina, 20020599) and sequenced on the NovaSeq 6000 instrument (Illumina). Each condition was performed with three biological replicates. Data processing, quality control, trimming, and mapping were performed using snakePipes mRNA-seq pipeline (*95*). Differential expression analysis was performed using DESeq2 with an FDR cutoff of 0.05 (*96*). GSEA and overrepresentation analysis were performed using the ClusterProfiler in R (*97*). Heatmaps of *z* score were generated using the pheatmap package in R.

ChIP sequencing

Fixed WT podocytes were FACS-sorted as described earlier, snap-frozen, and stored at −80°C until all samples were ready. MEFs infected with lentiviral overexpression constructs were trypsinized (trypsin-EDTA, Sigma T4049) and fixed in 1% PFA for 10 min at room temperature. Fixed cell pellets were washed with PBS, snap-frozen, and stored at −80°C until all samples were ready. Nuclei extraction, quantification, barcoding, multiplexing, and ChIP were performed using the RELACS protocol as previously described (*69*). Libraries were prepared using the NEBNext Ultra II DNA Library Prep Kit for Illumina (NEB, E7645) and sequenced on the NovaSeq 6000 instrument (Illumina). The antibodies used are listed in table S7. Each ChIP was performed with two biological replicates. Data processing, quality control, trimming, mapping, and H3-normalized coverage file were performed using snakePipes DNA-mapping and ChIP-seq pipeline (*95*). Further analysis and plotting were performed using deepTools (*98*). The output from "deepTools - ComputeMatrix" was used for boxplots. For H4K16ac, which is known for genebody enrichment, individual genes were fit into 1000 bins using the "ComputeMatrix-scale region" function of deepTools. For all other marks, TSS ± 500 bp were used.

Quantification and statistical analysis

Data are presented as means ± SEM or as indicated in the figure legends. The exact replicate numbers are mentioned in the respective method sections or figure legends. All statistical analyses were performed using Prism 9 software (GraphPad) unless otherwise specified. *P* values are shown directly. Nonsignificant *P* values are either not labeled or labeled as "ns." Details of statistical tests are reported in the figure legends and/or figures.

Supplementary Materials

This PDF file includes:
Figs. S1 to S6
Legends for tables S1 to S8

Other Supplementary Material for this manuscript includes the following:
Tables S1 to S8

REFERENCES AND NOTES

1. B. N. Sheikh, A. Akhtar, The many lives of KATs—Detectors, integrators and modulators of the cellular environment. *Nat. Rev. Genet.* **20**, 7–23 (2018).
2. X.-J. Yang, E. Seto, HATs and HDACs: From structure, function and regulation to novel strategies for therapy and prevention. *Oncogene* **26**, 5310–5318 (2007).
3. S. Timmermann, H. Lehrmann, A. Polesskaya, A. Harel-Bellan, Histone acetylation and disease. *Cell. Mol. Life Sci.* **58**, 728–736 (2001).
4. L. Li, M. Ghorbani, M. Weisz-Hubshman, J. Rousseau, I. Thiffault, R. E. Schnur, C. Breen, R. Oegema, M. M. Weiss, Q. Waisfisz, S. Welner, H. Kingston, J. A. Hills, E. M. Boon, L. Basel-Salmon, O. Konen, H. Goldberg-Stern, L. Bazak, S. Tzur, J. Jin, X. Bi, M. Bruccoleri, K. McWalter, M. T. Cho, M. Scarano, G. B. Schaefer, S. S. Brooks, S. S. Hughes, K. L. I. van Gassen, J. M. van Hagen, T. K. Pandita, P. B. Agrawal, P. M. Campeau, X.-J. Yang, Lysine acetyltransferase 8 is involved in cerebral development and syndromic intellectual disability. *J. Clin. Invest.* **130**, 1431–1445 (2020).
5. J. H. Roelfsema, S. J. White, Y. Ariyürek, D. Bartholdi, D. Niedrist, F. Papadia, C. A. Bacino, J. T. den Dunnen, G.-J. B. van Ommen, M. H. Breuning, R. C. Hennekam, D. J. M. Peters, Genetic heterogeneity in Rubinstein-Taybi syndrome: Mutations in both the CBP and EP300 genes cause disease. *Am. J. Hum. Genet.* **76**, 572–580 (2005).
6. A. Gupta, C. R. Hunt, R. K. Pandita, J. Pae, K. Komal, M. Singh, J. W. Shay, R. Kumar, K. Ariizumi, N. Horikoshi, W. N. Hittelman, C. Guha, T. Ludwig, T. K. Pandita, T-cell-specific deletion of Mof blocks their differentiation and results in genomic instability in mice. *Mutagenesis* **28**, 263–270 (2013).
7. R. Kumar, C. R. Hunt, A. Gupta, S. Nannepaga, R. K. Pandita, J. W. Shay, R. Bachoo, T. Ludwig, D. K. Burns, T. K. Pandita, Purkinje cell-specific males absent on the first (mMof) gene deletion results in an ataxia-telangiectasia-like neurological phenotype and backward walking in mice. *Proc. Natl. Acad. Sci. U.S.A.* **108**, 3636–3641 (2011).

8. D. A. Koolen, R. Pfundt, K. Linda, G. Beunders, H. E. Veenstra-Knol, J. H. Conta, A. M. Fortuna, G. Gillessen-Kaesbach, S. Dugan, S. Halbach, O. A. Abdul-Rahman, H. M. Winesett, W. K. Chung, M. Dalton, P. S. Dimova, T. Mattina, K. Prescott, H. Z. Zhang, H. M. Saal, J. Y. Hehir-Kwa, M. H. Willemsen, C. W. Ockeloen, M. C. Jongmans, N. Van der Aa, P. Failla, C. Barone, E. Avola, A. S. Brooks, S. G. Kant, E. H. Gerkes, H. V. Firth, K. Õunap, L. M. Bird, D. Masser-Frye, J. R. Friedman, M. A. Sokunbi, A. Dixit, M. Splitt, D. D. D. Study, M. K. Kukolich, J. McGaughran, B. P. Coe, J. Flórez, N. N. Kasri, H. G. Brunner, E. M. Thompson, J. Gecz, C. Romano, E. E. Eichler, B. B. A. de Vries, The Koolen-de Vries syndrome: A phenotypic comparison of patients with a 17q21.31 microdeletion versus a KANSL1 sequence variant. *Eur. J. Hum. Genet.* **24**, 652–659 (2016).
9. M. F. Basilicata, A.-L. Bruel, G. Semplicio, C. I. K. Valsecchi, T. Aktaş, Y. Duffourd, T. Rumpf, J. Morton, I. Bache, W. G. Szymanski, C. Gilissen, O. Vanakker, K. Õunap, G. Mittler, I. van der Burgt, S. El Chehadeh, M. T. Cho, R. Pfundt, T. Y. Tan, M. Kirchhoff, B. Menten, S. Vergult, K. Lindstrom, A. Reis, D. S. Johnson, A. Fryer, V. McKay, R. B. Fisher, C. Thauvin-Robinet, D. Francis, T. Roscioli, S. Pajusalu, K. Radtke, J. Ganesh, H. G. Brunner, M. Wilson, L. Faivre, V. M. Kalscheuer, J. Thevenon, A. Akhtar, De novo mutations in MSL3 cause an X-linked syndrome marked by impaired histone H4 lysine 16 acetylation. *Nat. Genet.* **50**, 1442–1451 (2018).
10. B. N. Sheikh, Crafting the brain—Role of histone acetyltransferases in neural development and disease. *Cell Tissue Res.* **356**, 553–573 (2014).
11. A. Gupta, T. G. Guerin-Peyrou, G. G. Sharma, C. Park, M. Agarwal, R. K. Ganju, S. Pandita, K. Choi, S. Sukumar, R. K. Pandita, T. Ludwig, T. K. Pandita, The mammalian ortholog of Drosophila MOF that acetylates histone H4 lysine 16 is essential for embryogenesis and oncogenesis. *Mol. Cell. Biol.* **28**, 397–409 (2008).
12. Y. Cai, J. Jin, S. K. Swanson, M. D. Cole, S. H. Choi, L. Florens, M. P. Washburn, J. W. Conaway, R. C. Conaway, Subunit composition and substrate specificity of a MOF-containing histone acetyltransferase distinct from the male-specific lethal (MSL) complex. *J. Biol. Chem.* **285**, 4268–4272 (2010).
13. A. Chatterjee, J. Seyfferth, J. Lucci, R. Gilsbach, S. Preissl, L. Böttinger, C. U. Mårtensson, A. Panhale, T. Stehle, O. Kretz, A. H. Sahyoun, S. Avilov, S. Eimer, L. Hein, N. Pfanner, T. Becker, A. Akhtar, MOF acetyl transferase regulates transcription and respiration in mitochondria. *Cell* **167**, 722–738.e23 (2016).
14. A. Karoutas, W. Szymanski, T. Rausch, S. Guhathakurta, E. A. Rog-Zielinska, R. Peyronnet, J. Seyfferth, H.-R. Chen, R. de Leeuw, B. Herquel, H. Kimura, G. Mittler, P. Kohl, O. Medalia, J. O. Korbel, A. Akhtar, The NSL complex maintains nuclear architecture stability via lamin A/C acetylation. *Nat. Cell Biol.* **21**, 1248–1260 (2019).
15. J. Dias, N. Van Nguyen, P. Georgiev, A. Gaub, J. Brettschneider, S. Cusack, J. Kadlec, A. Akhtar, Structural analysis of the KANSL1/WDR5/KANSL2 complex reveals that WDR5 is required for efficient assembly and chromatin targeting of the NSL complex. *Genes Dev.* **28**, 929–942 (2014).
16. S. Mendjan, M. Taipale, J. Kind, H. Holz, P. Gebhardt, M. Schelder, M. Vermeulen, A. Buscaino, K. Duncan, J. Mueller, M. Wilm, H. G. Stunnenberg, H. Saumweber, A. Akhtar, Nuclear pore components are involved in the transcriptional regulation of dosage compensation in Drosophila. *Mol. Cell* **21**, 811–823 (2006).
17. D. S. Andersen, S. J. Raja, J. Colombani, R. L. Shaw, P. F. Langton, A. Akhtar, N. Tapon, Drosophila MCRS2 associates with RNA polymerase II complexes to regulate transcription. *Mol. Cell. Biol.* **30**, 4744–4755 (2010).
18. K. C. Lam, H.-R. Chung, G. Semplicio, S. S. Iyer, A. Gaub, V. Bhardwaj, H. Holz, P. Georgiev, A. Akhtar, The NSL complex–mediated nucleosome landscape is required to maintain transcription fidelity and suppression of transcription noise. *Genes Dev.* **33**, 452–465 (2019).
19. K. C. Lam, F. Mühlpfordt, J. M. Vaquerizas, S. J. Raja, H. Holz, N. M. Luscombe, T. Manke, A. Akhtar, The NSL complex regulates housekeeping genes in Drosophila. *PLOS Genet.* **8**, e1002736 (2012).
20. C. Feller, M. Prestel, H. Hartmann, T. Straub, J. Söding, P. B. Becker, The MOF-containing NSL complex associates globally with housekeeping genes, but activates only a defined subset. *Nucleic Acids Res.* **40**, 1509–1522 (2012).
21. S. J. Raja, I. Charapitsa, T. Conrad, J. M. Vaquerizas, P. Gebhardt, H. Holz, J. Kadlec, S. Fraterman, N. M. Luscombe, A. Akhtar, The nonspecific lethal complex is a transcriptional regulator in Drosophila. *Mol. Cell* **38**, 827–841 (2010).
22. T. Chelmicki, F. Dündar, M. J. Turley, T. Khanam, T. Aktas, F. Ramírez, A.-V. Gendrel, P. R. Wright, P. Videm, R. Backofen, E. Heard, T. Manke, A. Akhtar, MOF-associated complexes ensure stem cell identity and Xist repression. *eLife* **3**, e02024 (2014).
23. A. Gaub, B. N. Sheikh, M. F. Basilicata, M. Vincent, M. Nizon, C. Colson, M. J. Bird, J. E. Bradner, J. Thevenon, M. Boutros, A. Akhtar, Evolutionary conserved NSL complex/BRD4 axis controls transcription activation via histone acetylation. *Nat. Commun.* **11**, 1–17 (2020).
24. C. P. Rodrigues, J. S. Herman, B. Herquel, C. I. K. Valsecchi, T. Stehle, D. Grün, A. Akhtar, Temporal expression of MOF acetyltransferase primes transcription factor networks for erythroid fate. *Sci. Adv.* **6**, eaaz4815 (2020).
25. C. Pessoa Rodrigues, A. Akhtar, Differential H4K16ac levels ensure a balance between quiescence and activation in hematopoietic stem cells. *Sci. Adv.* **7**, eabi5987 (2021).
26. B. N. Sheikh, S. Guhathakurta, T. H. Tsang, M. Schwabenland, G. Renschler, B. Herquel, V. Bhardwaj, H. Holz, T. Stehle, O. Bondareva, N. Aizarani, O. Mossad, O. Kretz, W. Reichardt, A. Chatterjee, L. J. Braun, J. Thevenon, H. Sartelet, T. Blank, D. Grün, D. von Elverfeldt, T. B. Huber, D. Vestweber, S. Avilov, M. Prinz, J. M. Buescher, A. Akhtar, Neural metabolic imbalance induced by MOF dysfunction triggers pericyte activation and breakdown of vasculature. *Nat. Cell Biol.* **22**, 828–841 (2020).
27. B. N. Sheikh, W. Bechtel-Walz, J. Lucci, O. Karpiuk, I. Hild, B. Hartleben, J. Vornweg, M. Helmstädter, A. H. Sahyoun, V. Bhardwaj, T. Stehle, S. Diehl, O. Kretz, A. K. Voss, T. Thomas, T. Manke, T. B. Huber, A. Akhtar, MOF maintains transcriptional programs regulating cellular stress response. *Oncogene* **35**, 2698–2710 (2016).
28. J. S. Lin, K. Susztak, Podocytes: The weakest link in diabetic kidney disease? *Curr. Diab. Rep.* **16**, 45 (2016).
29. C. Schell, T. B. Huber, The evolving complexity of the podocyte cytoskeleton. *J. Am. Soc. Nephrol.* **28**, 3166–3174 (2017).
30. P. M. Andrews, S. B. Bates, Filamentous actin bundles in the kidney. *Anat. Rec.* **210**, 1–9 (1984).
31. D. Drenckhahn, R. P. Franke, Ultrastructural organization of contractile and cytoskeletal proteins in glomerular podocytes of chicken, rat, and man. *Lab. Invest.* **59**, 673–682 (1988).
32. H. Fukasawa, S. Bornheimer, K. Kudlicka, M. G. Farquhar, Slit diaphragms contain tight junction proteins. *J. Am. Soc. Nephrol.* **20**, 1491–1503 (2009).
33. M. K. Kocylowski, H. Aypek, W. Bildl, M. Helmstädter, P. Trachte, B. Dumoulin, S. Wittösch, L. Kühne, U. Aukschun, C. Teetzen, O. Kretz, B. Gaal, A. Kulik, C. Antignac, G. Mollet, A. Köttgen, B. Göcmen, J. Schwenk, U. Schulte, T. B. Huber, B. Fakler, F. Grahammer, A slit-diaphragm-associated protein network for dynamic control of renal filtration. *Nat. Commun.* **13**, 1–15 (2022).
34. H. Yuan, E. Takeuchi, D. J. Salant, Podocyte slit-diaphragm protein nephrin is linked to the actin cytoskeleton. *Am. J. Physiol. Renal Physiol.* **282**, F585–F591 (2002).
35. C. R. Neal, Podocytes ... what's under yours? (podocytes and foot processes and how they change in nephropathy). *Front. Endocrinol.* **6**, 9 (2015).
36. S. Meunier, M. Shvedunova, N. Van Nguyen, L. Avila, I. Vernos, A. Akhtar, An epigenetic regulator emerges as microtubule minus-end binding and stabilizing factor in mitosis. *Nat. Commun.* **6**, 1–10 (2015).
37. C. Schell, B. Sabass, M. Helmstaedter, F. Geist, A. Abed, M. Yasuda-Yamahara, A. Sigle, J. I. Maier, F. Grahammer, F. Siegerist, N. Artelt, N. Endlich, D. Kerjaschki, H.-H. Arnold, J. Dengjel, M. Rogg, T. B. Huber, ARP3 controls the podocyte architecture at the kidney filtration barrier. *Dev. Cell* **47**, 741–757.e8 (2018).
38. I. Refaeli, M. R. Hughes, A. K.-W. Wong, M. L. Z. Bissonnette, C. D. Roskelley, A. W. Vogl, S. J. Barbour, B. S. Freedman, K. M. McNagny, Distinct functional requirements for podocalyxin in immature and mature podocytes reveal mechanisms of human kidney disease. *Sci. Rep.* **10**, 1–14 (2020).
39. M. J. Moeller, S. K. Sanden, A. Soofi, R. C. Wiggins, L. B. Holzman, Podocyte-specific expression of cre recombinase in transgenic mice. *Genesis* **35**, 39–42 (2003).
40. M. G. Betjes, Uremia-associated ageing of the thymus and adaptive immune responses. *Toxins* **12**, 224 (2020).
41. K. Iio, D. Kabata, R. Iio, Y. Imai, M. Hatanaka, H. Omori, Y. Hoshida, Y. Saeki, A. Shintani, T. Hamano, Y. Isaka, Y. Ando, Parathyroid hormone and premature thymus ageing in patients with chronic kidney disease. *Sci. Rep.* **9**, 1–8 (2019).
42. K. Ichimura, H. Kurihara, T. Sakai, Primary cilia disappear in rat podocytes during glomerular development. *Cell Tissue Res.* **341**, 197–209 (2010).
43. J. F. Reiter, M. R. Leroux, Genes and molecular pathways underpinning ciliopathies. *Nat. Rev. Mol. Cell Biol.* **18**, 533–547 (2017).
44. F. Finetti, S. R. Paccani, M. G. Riparbelli, E. Giacomello, G. Perinetti, G. J. Pazour, J. L. Rosenbaum, C. T. Baldari, Intraflagellar transport is required for polarized recycling of the TCR/CD3 complex to the immune synapse. *Nat. Cell Biol.* **11**, 1332–1339 (2009).
45. B. N. Sheikh, S. Guhathakurta, A. Akhtar, The non-specific lethal (NSL) complex at the crossroads of transcriptional control and cellular homeostasis. *EMBO Rep.* **20**, e47630 (2019).
46. M. Taipale, S. Rea, K. Richter, A. Vilar, P. Lichter, A. Imhof, A. Akhtar, hMOF histone acetyltransferase is required for histone H4 lysine 16 acetylation in mammalian cells. *Mol. Cell. Biol.* **25**, 6798–6810 (2005).
47. A. Grochowsky, M. Gunay-Aygun, Clinical characteristics of individual organ system disease in non-motile ciliopathies. *Transl. Sci. Rare Dis.* **4**, 1–23 (2019).
48. A. Radzisheuskaya, P. V. Shliaha, V. V. Grinev, D. Shlyueva, H. Damhofer, R. Koche, V. Gorshkov, S. Kovalchuk, Y. Zhan, K. L. Rodriguez, A. L. Johnstone, M.-C. Keogh, R. C. Hendrickson, O. N. Jensen, K. Helin, Complex-dependent histone acetyltransferase activity of KAT8 determines its role in transcription and cellular homeostasis. *Mol. Cell* **81**, 1749–1765.e8 (2021).

49. M. N. H. Luijten, S. G. Basten, T. Claessens, M. Vernooij, C. L. Scott, R. Janssen, J. A. Easton, M. A. F. Kamps, M. Vreeburg, J. L. V. Broers, M. van Geel, F. H. Menko, R. P. Harbottle, R. K. Nookala, A. R. Tee, S. C. Land, R. H. Giles, B. J. Coull, M. A. M. van Steensel, Birt–H-ogg–Dubé syndrome is a novel ciliopathy. *Hum. Mol. Genet.* **22**, 4383–4397 (2013).
50. V. Marion, D. Schlicht, A. Mockel, S. Caillard, O. Imhoff, C. Stoetzel, P. van Dijk, C. Brandt, B. Moulin, H. Dollfus, Bardet–Biedl syndrome highlights the major role of the primary cilium in efficient water reabsorption. *Kidney Int.* **79**, 1013–1025 (2011).
51. D. Iaconis, C. Crina, S. Brillante, A. Indrieri, M. Morleo, B. Franco, The HOPS complex subunit VPS39 controls ciliogenesis through autophagy. *Hum. Mol. Genet.* **29**, 1018–1029 (2020).
52. E. D. Gigante, M. R. Taylor, A. A. Ivanova, R. A. Kahn, T. Caspary, ARL13B regulates Sonic hedgehog signaling from outside primary cilia. *eLife* **9**, e50434 (2020).
53. M. Delling, P. G. DeCaen, J. F. Doerner, S. Febvay, D. E. Clapham, Primary cilia are specialized calcium signalling organelles. *Nature* **504**, 311–314 (2013).
54. B. T. Keady, R. Samtani, K. Tobita, M. Tsuchya, J. T. San Agustin, J. A. Follit, J. A. Jonassen, R. Subramanian, C. W. Lo, G. J. Pazour, IFT25 links the signal-dependent movement of Hedgehog components to intraflagellar transport. *Dev. Cell* **22**, 940–951 (2012).
55. F. Bangs, K. V. Anderson, Primary cilia and mammalian hedgehog signaling. *Cold Spring Harb. Perspect. Biol.* **9**, a028175 (2017).
56. C. Schell, L. Baumhakl, S. Salou, A.-C. Conzelmann, C. Meyer, M. Helmstädter, C. Wrede, F. Grahammer, S. Eimer, D. Kerjaschki, G. Walz, S. Snapper, T. B. Huber, N-wasp is required for stabilization of podocyte foot processes. *J. Am. Soc. Nephrol.* **24**, 713–721 (2013).
57. T. Struk, V. Nair, F. Eichinger, M. Kretzler, R. Wedlich-Söldner, S. Bayraktar, H. Pavenstädt, Transcriptome analysis of primary podocytes reveals novel calcium regulated regulatory networks. *FASEB J.* **34**, 14490–14506 (2020).
58. O. Lenoir, M. Jasiek, C. Hénique, L. Guyonnet, B. Hartleben, T. Bork, A. Chipont, K. Flosseau, I. Bensaada, A. Schmitt, J.-M. Massé, M. Souyri, T. B. Huber, P.-L. Tharaux, Endothelial cell and podocyte autophagy synergistically protect from diabetes-induced glomerulosclerosis. *Autophagy* **11**, 1130–1145 (2015).
59. S. Chittiprol, P. Chen, D. Petrovic-Djergovic, T. Eichler, R. F. Ransom, Marker expression, behaviors, and responses vary in different lines of conditionally immortalized cultured podocytes. *Am. J. Physiol. Renal Physiol.* **301**, F660–F671 (2011).
60. Z.-H. Li, X.-Y. Guo, X.-Y. Quan, C. Yang, Z.-J. Liu, H.-Y. Su, N. An, H.-F. Liu, The role of parietal epithelial cells in the pathogenesis of podocytopathy. *Front. Physiol.* **13**, 832772 (2022).
61. L. Kietzmann, S. S. O. Guhr, T. N. Meyer, L. Ni, M. Sachs, U. Panzer, R. A. K. Stahl, M. A. Saleem, D. Kerjaschki, C. A. Gebeshuber, C. Meyer-Schwesinger, MicroRNA-193a regulates the transdifferentiation of human parietal epithelial cells toward a podocyte phenotype. *J. Am. Soc. Nephrol.* **26**, 1389–1401 (2015).
62. E. Ronconi, C. Sagrinati, M. L. Angelotti, E. Lazzeri, B. Mazzinghi, L. Ballerini, E. Parente, F. Becherucci, M. Gacci, M. Carini, E. Maggi, M. Serio, G. B. Vannelli, L. Lasagni, S. Romagnani, P. Romagnani, Regeneration of glomerular podocytes by human renal progenitors. *J. Am. Soc. Nephrol.* **20**, 322–332 (2009).
63. F. A. Hatje, U. Wedekind, W. Sachs, D. Loreth, J. Reichelt, F. Demir, C. Kosub, L. Heintz, N. M. Tomas, T. B. Huber, S. Skuza, M. Sachs, S. Zielinski, M. M. Rinschen, C. Meyer-Schwesinger, Tripartite separation of glomerular cell types and proteomes from reporter-free mice. *J. Am. Soc. Nephrol.* **32**, 2175–2193 (2021).
64. J.-J. Chung, L. Goldstein, Y.-J. J. Chen, J. Lee, J. D. Webster, M. Roose-Girma, S. C. Paudyal, Z. Modrusan, A. Dey, A. S. Shaw, Single-cell transcriptome profiling of the kidney glomerulus identifies key cell types and reactions to injury. *J. Am. Soc. Nephrol.* **31**, 2341–2354 (2020).
65. D. Zhou, H. Fu, Y. Han, L. Zhang, S. Liu, L. Lin, D. B. Stolz, Y. Liu, Sonic hedgehog connects podocyte injury to mesangial activation and glomerulosclerosis. *JCI Insight* **4**, e130515 (2019).
66. E. Huynh Cong, A. A. Bizet, O. Boyer, S. Woerner, O. Gribouval, E. Filhol, C. Arrondel, S. Thomas, F. Silbermann, G. Canaud, J. Hachicha, N. Ben Dhia, M.-N. Peraldi, K. Harzallah, D. Iftene, L. Daniel, M. Willems, L.-H. Noel, C. Bole-Feysot, P. Nitschké, M.-C. Gubler, G. Mollet, S. Saunier, C. Antignac, A homozygous missense mutation in the ciliary gene TTC21B causes familial FSGS. *J. Am. Soc. Nephrol.* **25**, 2435–2443 (2014).
67. S. Yu, W.-I. Choi, Y. J. Choi, H.-Y. Kim, F. Hildebrandt, H. Y. Gee, PLCE1 regulates the migration, proliferation, and differentiation of podocytes. *Exp. Mol. Med.* **52**, 594–603 (2020).
68. E. Widmeier, W. Tan, M. Airik, F. Hildebrandt, A small molecule screening to detect potential therapeutic targets in human podocytes. *Am. J. Physiol. Renal Physiol.* **312**, F157–F171 (2017).
69. L. Arrigoni, H. Al-Hasani, F. Ramírez, I. Panzeri, D. P. Ryan, D. Santacruz, N. Kress, J. A. Pospisilik, U. Bönisch, T. Manke, RELACS nuclei barcoding enables high-throughput ChIP-seq. *Commun. Biol.* **1**, 214 (2018).
70. R. A. Henry, Y.-M. Kuo, A. J. Andrews, Differences in specificity and selectivity between CBP and p300 acetylation of histone H3 and H3/H4. *Biochemistry* **52**, 5746–5759 (2013).
71. C. Feller, I. Forné, A. Imhof, P. B. Becker, Global and specific responses of the histone acetylome to systematic perturbation. *Mol. Cell* **57**, 559–571 (2015).
72. A. Kimura, M. Horikoshi, Tip60 acetylates six lysines of a specific class in core histones in vitro. *Genes Cells* **3**, 789–800 (1998).
73. B. T. Weinert, T. Narita, S. Satpathy, B. Srinivasan, B. K. Hansen, C. Schölz, W. B. Hamilton, B. E. Zucconi, W. W. Wang, W. R. Liu, J. M. Brickman, E. A. Kesicki, A. Lai, K. D. Bromberg, P. A. Cole, C. Choudhary, Time-resolved analysis reveals rapid dynamics and broad scope of the CBP/p300 acetylome. *Cell* **174**, 231–244.e12 (2018).
74. S. Guelman, K. Kozuka, Y. Mao, V. Pham, M. J. Solloway, J. Wang, J. Wu, J. R. Lill, J. Zha, The double-histone-acetyltransferase complex ATAC is essential for mammalian development. *Mol. Cell. Biol.* **29**, 1176–1188 (2009).
75. O. Leon, M. Roth, Zinc fingers: DNA binding and protein-protein interactions. *Biol. Res.* **33**, 21–30 (2000).
76. A. Robert, G. Margall-Ducos, J.-E. Guidotti, O. Brégerie, C. Celati, C. Bréchot, C. Desdouets, The intraflagellar transport component IFT88/polaris is a centrosomal protein regulating G1-S transition in non-ciliated cells. *J. Cell Sci.* **120**, 628–637 (2007).
77. T. Sedmak, U. Wolfrum, Intraflagellar transport molecules in ciliary and nonciliary cells of the retina. *J. Cell Biol.* **189**, 171–186 (2010).
78. M. A. Dupont, C. Humbert, C. Huber, Q. Siour, I. C. Guerrera, V. Jung, A. Christensen, A. Pouliet, M. Garfa-Traoré, P. Nitschké, M. Injeyan, K. Millar, D. Chitayat, P. Shannon, K. M. Girisha, A. Shukla, C. Mechler, E. Lorentzen, A. Benmerah, V. Cormier-Daire, C. Jeanpierre, S. Saunier, M. Delous, Human IFT52 mutations uncover a novel role for the protein in microtubule dynamics and centrosome cohesion. *Hum. Mol. Genet.* **28**, 2720–2737 (2019).
79. H. Shi, S. Chen, H. Jin, C. Xu, G. Dong, Q. Zhao, W. Wang, H. Zhang, W. Lin, J. Zhang, L. Davidovic, L. Yao, D. Fan, Downregulation of MSP58 inhibits growth of human colorectal cancer cells via regulation of the cyclin D1-cyclin-dependent kinase 4-p21 pathway. *Cancer Sci.* **100**, 1585–1590 (2009).
80. N. E. Ferreyra Solari, F. S. Belforte, L. Canedo, G. A. Videla-Richardson, J. M. Espinosa, M. Rossi, E. Serna, M. A. Riudavets, H. Martinetto, G. Sevlever, C. Perez-Castro, The NSL chromatin-modifying complex subunit KANSL2 regulates cancer stem-like properties in glioblastoma that contribute to tumorigenesis. *Cancer Res.* **76**, 5383–5394 (2016).
81. P. O. Oladimeji, J. Bakke, W. C. Wright, T. Chen, KANSL2 and MBNL3 are regulators of pancreatic ductal adenocarcinoma invasion. *Sci. Rep.* **10**, 1–8 (2020).
82. J.-S. Chen, X.-H. Huang, Q. Wang, J.-Q. Huang, L.-J. Zhang, X.-L. Chen, J. Lei, Z.-X. Cheng, Sonic hedgehog signaling pathway induces cell migration and invasion through focal adhesion kinase/AKT signaling-mediated activation of matrix metalloproteinase (MMP)-2 and MMP-9 in liver cancer. *Carcinogenesis* **34**, 10–19 (2012).
83. A. Wiegering, U. Rüther, C. Gerhardt, The role of hedgehog signalling in the formation of the ventricular septum. *J. Dev. Biol.* **5**, 17 (2017).
84. D. P. Gupta, J.-W. Hwang, E.-S. Cho, W. Kim, C. H. Song, O. H. Chai, Constitutive activation of smoothened in the renal collecting ducts leads to renal hypoplasia, hydronephrosis, and hydroureter. *Cells Tissues Organs* **204**, 38–48 (2017).
85. V. M. Kozlov, A. Schedl, Duplex kidney formation: Developmental mechanisms and genetic predisposition. *F1000Res.* **9**, F1000 (2020).
86. P. B. Desai, J. T. San Agustin, M. W. Stuck, J. A. Jonassen, C. M. Bates, G. J. Pazour, Ift25 is not a cystic kidney disease gene but is required for early steps of kidney development. *Mech. Dev.* **151**, 10–17 (2018).
87. S. Ettou, Y. L. Jung, T. Miyoshi, D. Jain, K. Hiratsuka, V. Schumacher, M. E. Taglienti, R. Morizane, P. J. Park, J. A. Kreidberg, Epigenetic transcriptional reprogramming by WT1 mediates a repair response during podocyte injury. *Sci. Adv.* **6**, eabb5460 (2020).
88. K. Inoue, G. Gan, M. Ciarleglio, Y. Zhang, X. Tian, C. E. Pedigo, C. Cavanaugh, J. Tate, Y. Wang, E. Cross, M. Groener, N. Chai, Z. Wang, A. Justice, Z. Zhang, C. R. Parikh, F. P. Wilson, S. Ishibe, Podocyte histone deacetylase activity regulates murine and human glomerular diseases. *J. Clin. Invest.* **129**, 1295–1313 (2019).
89. S. J. Shankland, J. W. Pippin, J. Reiser, P. Mundel, Podocytes in culture: Past, present, and future. *Kidney Int.* **72**, 26–36 (2007).
90. J. Wichmann, C. Pitt, S. Eccles, A. L. Garnham, C. S. N. Li-Wai-Suen, R. May, E. Allan, S. Wilcox, M. J. Herold, G. K. Smyth, B. J. Monahan, T. Thomas, A. K. Voss, Loss of TIP60 (KAT5) abolishes H2AZ lysine 7 acetylation and causes p53, INK4A, and ARF-independent cell cycle arrest. *Cell Death Dis.* **13**, 627 (2022).
91. E. L. Huttlin, R. J. Bruckner, J. Navarrete-Perea, J. R. Cannon, K. Baltier, F. Gebreab, M. P. Gygi, A. Thornock, G. Zarraga, S. Tam, J. Szpyt, B. M. Gassaway, A. Panov, H. Parzen, S. Fu, A. Golbazi, E. Maenpaa, K. Stricker, S. Guha Thakurta, T. Zhang, R. Rad, J. Pan, D. P. Nusinow, J. A. Paulo, D. K. Schweppe, L. P. Vaites, J. W. Harper, S. P. Gygi, Dual proteome-scale networks reveal cell-specific remodeling of the human interactome. *Cell* **184**, 3022–3040.e28 (2021).
92. A. Tasca, M. Helmstädter, M. Brislinger, M. Haas, P. Walentek, A changing signaling environment induces multiciliated cell trans-differentiation during developmental remodeling. bioRxiv 2020.04.16.045401 [Preprint]. 18 April 2020. https://doi.org/10.1101/2020.04.16.045401.

93. A. Suarez-Arnedo, F. Torres Figueroa, C. Clavijo, P. Arbeláez, J. C. Cruz, C. Muñoz-Camargo, An image J plugin for the high throughput image analysis of in vitro scratch wound healing assays. *PLOS ONE* **15**, e0232565 (2020).
94. C. Li, H. M. Siragy, High glucose induces podocyte injury via enhanced (pro)renin receptor-Wnt-β-catenin-snail signaling pathway. *PLOS ONE* **9**, e89233 (2014).
95. V. Bhardwaj, S. Heyne, K. Sikora, L. Rabbani, M. Rauer, F. Kilpert, A. S. Richter, D. P. Ryan, T. Manke, snakePipes: Facilitating flexible, scalable and integrative epigenomic analysis. *Bioinformatics* **35**, 4757–4759 (2019).
96. M. I. Love, W. Huber, S. Anders, Moderated estimation of fold change and dispersion for RNA-seq data with DESeq2. *Genome Biol.* **15**, 550 (2014).
97. G. Yu, L.-G. Wang, Y. Han, Q.-Y. He, clusterProfiler: An R package for comparing biological themes among gene clusters. *OMICS* **16**, 284–287 (2012).
98. F. Ramírez, F. Dündar, S. Diehl, B. A. Grüning, T. Manke, deepTools: A flexible platform for exploring deep-sequencing data. *Nucleic Acids Res.* **42**, W187–W191 (2014).

Acknowledgments: We are grateful to B. N. Sheikh for valuable support in supervision and guidance; C. P. Rodrigues, G. V. Renschler, and Y. D. Sun for sharing bioinformatic knowledge; S. Kayser for technical assistance; M. E. Akbas for assistance in the creation of the model; and the MPI-IE core facilities for FACS, deep sequencing, mouse, and imaging, which have been invaluable for this project. The work of S. Kayser and M.H. was performed at the Core Facility for Electron Microscopy [EMcore (RI_00555)] at the University Freiburg Medical Center - IMITATE, Germany. BioRender.com was used to create certain panels. **Funding:** This study was supported by the German Research Foundation (DFG) under Germany's Excellence Strategy (CIBSS – EXC-2189 – Project ID 390939984) awarded to A.A. This work was also supported by the German Research Foundation (DFG) under the CRC 992 (A02), CRC 1425 (P04), and CRC 1381 (B3) awarded to A.A. **Author contributions:** Conceptualization: T.H.T. and A.A. Methodology: T.H.T. Investigation: T.H.T., M.W., M.H., T.S., J.S., and H.H. Animal breeding and handling: T.H.T. and T.S. Analysis: T.H.T. Visualization: T.H.T. Writing: T.H.T., M.S., and A.A. Funding acquisition: A.A. Supervision: G.W. and A.A. **Competing interests:** The authors declare that they have no competing interests. **Data and materials availability:** All data needed to evaluate the conclusions in the paper are present in the paper and/or the Supplementary Materials. The raw data from RNA-seq and ChIP-seq experiments have been uploaded to GEO with the accession number GSE225434. RNA-seq data from human THP-1 cells were obtained from GEO with the accession number GSE158521 (*48*). Processed proteomics data were obtained from (*48*) and were directly used for visualization.

Submitted 12 March 2023
Accepted 25 July 2023
Published 25 August 2023
10.1126/sciadv.adh5598

ScienceAdvances

Transcriptional regulation by the NSL complex enables diversification of IFT functions in ciliated versus nonciliated cells

Tsz Hong Tsang, Meike Wiese, Martin Helmstädter, Thomas Stehle, Janine Seyfferth, Maria Shvedunova, Herbert Holz, Gerd Walz, and Asifa Akhtar

Sci. Adv., **9** (34), eadh5598.
DOI: 10.1126/sciadv.adh5598